Prominent Mid-infrared Excess of the Dwarf Planet (136472) Makemake Discovered by JWST/MIRI Indicates Ongoing Activity

Csaba Kiss, Thomas G. Müller, Anikó Farkas-Takács, Attila Moór, Silvia Protopapa, Alex H. Parker, Pablo Santos-Sanz, Jose Luis Ortiz, Bryan J. Holler, Ian Wong, et al.

▶ **To cite this version:**

Csaba Kiss, Thomas G. Müller, Anikó Farkas-Takács, Attila Moór, Silvia Protopapa, et al.. Prominent Mid-infrared Excess of the Dwarf Planet (136472) Makemake Discovered by JWST/MIRI Indicates Ongoing Activity. The Astrophysical Journal Letters, 2024, 976, ⟨10.3847/2041-8213/ad8dcb⟩. ⟨insu-04853399⟩

HAL Id: insu-04853399

https://insu.hal.science/insu-04853399v1

Submitted on 24 Dec 2024

HAL is a multi-disciplinary open access archive for the deposit and dissemination of scientific research documents, whether they are published or not. The documents may come from teaching and research institutions in France or abroad, or from public or private research centers.

L'archive ouverte pluridisciplinaire **HAL**, est destinée au dépôt et à la diffusion de documents scientifiques de niveau recherche, publiés ou non, émanant des établissements d'enseignement et de recherche français ou étrangers, des laboratoires publics ou privés.

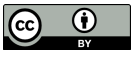

Distributed under a Creative Commons CC BY 4.0 - Attribution - International License

The Astrophysical Journal Letters, 976:L9 (16pp), 2024 November 20 https://doi.org/10.3847/2041-8213/ad8dcb
© 2024. The Author(s). Published by the American Astronomical Society.
OPEN ACCESS

Prominent Mid-infrared Excess of the Dwarf Planet (136472) Makemake Discovered by JWST/MIRI Indicates Ongoing Activity

Csaba Kiss[1,2,3], Thomas G. Müller[4], Anikó Farkas-Takács[1,2], Attila Moór[1,2], Silvia Protopapa[5], Alex H. Parker[6], Pablo Santos-Sanz[7], Jose Luis Ortiz[7], Bryan J. Holler[8], Ian Wong[9], John Stansberry[8], Estela Fernández-Valenzuela[10], Christopher R. Glein[11], Emmanuel Lellouch[12], Esa Vilenius[13], Csilla E. Kalup[1,2,3], Zsolt Regály[1,2], Róbert Szakáts[1,2], Gábor Marton[1,2], András Pál[1,2,3], and Gyula M. Szabó[14,15]
[1] Konkoly Observatory, HUN-REN Research Centre for Astronomy and Earth Sciences, Konkoly Thege 15-17, 1121 Budapest, Hungary; kiss.csaba@csfk.org
[2] CSFK, MTA Centre of Excellence, Konkoly Thege 15-17, 1121, Budapest, Hungary
[3] ELTE Eötvös Loránd University, Institute of Physics and Astronomy, Pázmány Péter sétány 1/A, 1171 Budapest, Hungary
[4] Max-Planck-Institut für extraterrestrische Physik, Giessenbachstr. 1, 85748 Garching, Germany
[5] Southwest Research Institute, 1301 Walnut Street, Suite 400, Boulder, CO 80302, USA
[6] SETI Institute, Mountain View, CA, USA
[7] Instituto de Astrofísica de Andalucía (CSIC), Glorieta de la Astronomía s/n, 18008 Granada, Spain
[8] Space Telescope Science Institute, 3700 San Martin Drive, Baltimore, MD 21218, USA
[9] NASA Goddard Space Flight Center, Greenbelt, MD 20771, USA
[10] Florida Space Institute, University of Central Florida, 12354 Research Parkway, Orlando, FL 32826, USA
[11] Space Science Division, Space Sector, Southwest Research Institute, 6220 Culebra Road, San Antonio, TX 78238-5166, USA
[12] LESIA, Observatoire de Paris, PSL Research University, CNRS, Sorbonne Université, UPMC Univ. Paris 06, Univ. Paris Diderot, Sorbonne Paris Cité, 5 place Jules Janssen, 92195 Meudon, France
[13] Mullard Space Science Laboratory, University College London, Holmbury St Mary, Dorking, Surrey, RH5 6NT, UK
[14] ELTE Eötvös Loránd University, Gothard Astrophysical Observatory, Szombathely, Hungary
[15] MTA-ELTE Exoplanet Research Group, 9700 Szombathely, Szent Imre h. u. 112, Hungary
Received 2024 October 9; revised 2024 October 28; accepted 2024 October 28; published 2024 November 14

Abstract

We report on the discovery of a very prominent mid-infrared (18–25 μm) excess associated with the trans-Neptunian dwarf planet (136472) Makemake. The excess, detected by the Mid-Infrared Instrument of the James Webb Space Telescope, along with previous measurements from the Spitzer and Herschel space telescopes, indicates the occurrence of temperatures of ∼150 K, much higher than what solid surfaces at Makemake's heliocentric distance could reach by solar irradiation. We identify two potential explanations: a continuously visible, currently active region powered by subsurface upwelling and possibly cryovolcanic activity covering $\leqslant$1% of Makemake's surface or an as-yet-undetected ring containing very small carbonaceous dust grains, which have not been seen before in trans-Neptunian or Centaur rings. Both scenarios point to unprecedented phenomena among trans-Neptunian objects and could greatly impact our understanding of these distant worlds.

Unified Astronomy Thesaurus concepts: Trans-Neptunian objects (1705); Classical Kuiper belt objects (250); Planetary rings (1254); Asteroid surfaces (2209); Planetary thermal histories (2290)

1. Introduction

(136472) Makemake is one of the largest and brightest objects in the Kuiper Belt. J. L. Ortiz et al. (2012) derived a size and albedo for Makemake from occultation measurements and obtained an equivalent diameter of ∼1430 km, an intermediate size between that of Pluto/Eris and Charon. They also found a bright surface with a geometric albedo of $p_V \approx 0.8$. The surface is known to be predominantly covered by methane (CH_4) ice (M. E. Brown et al. 2007; A. Alvarez-Candal et al. 2020) and by CH_4 irradiation products (M. E. Brown et al. 2015). W. M. Grundy et al. (2024) report that the D/H ratio in CH_4 ice observed on Makemake is significantly lower than that detected in comet 67P/Churyumov–Gerasimenko, which is considered to be primordial. However, it aligns closely with the ratios found in water in many comets and larger outer solar system objects. These similarities and differences prompted C. R. Glein et al. (2024) to suggest that the hydrogen atoms in CH_4 on Makemake originated from water, generated by geochemical processes at elevated temperatures in the deep interior. While there are several features on the surface of trans-Neptunian objects indicating past cryovolcanism (see A. Guilbert-Lepoutre et al. 2020 for a summary), ongoing activity has not been observed so far.

Thermal emission measurements in the infrared (IR) are traditionally used to obtain the size and albedo of solar system bodies (T. Müller et al. 2020). In addition, they also put constraints on the object's thermal properties and spin-axis orientations. The integration of multiwavelength and multi-technique data enhances the physical and thermal characterization of trans-Neptunian objects. This comprehensive approach allows for the inclusion of additional components, such as satellites and rings, and helps constrain properties that are otherwise inaccessible (see, e.g., E. Lellouch et al. 2017; T. Müller et al. 2019; C. Kiss et al. 2024).

The thermal emission of Makemake was first measured by the Spitzer Space Telescope (J. Stansberry et al. 2008) and then by the Herschel Space Observatory in the Science Demonstration Phase (SDP; T. L. Lim et al. 2010). To fit the observed flux densities, T. L. Lim et al. (2010) proposed a double-terrain model. A dark/warm component was necessary in addition to the general cold/high-albedo surface to account for the excess

Original content from this work may be used under the terms of the Creative Commons Attribution 4.0 licence. Any further distribution of this work must maintain attribution to the author(s) and the title of the work, journal citation and DOI.

observed by the Spitzer/Multiband Imaging Photometer (MIPS) at 24 μm. It was also suggested that the dark terrain might represent a satellite that was unknown at the time. A. H. Parker et al. (2016) detected a satellite using Hubble Space Telescope measurements that was 7.80 mag fainter than the primary. They proposed that this satellite might contribute to the 24 μm excess emission. By means of the Near-Earth Asteroid Thermal Model (NEATM; see, e.g., E. Lellouch et al. 2013), they found that to match the observed flux densities, the satellite contribution required a beaming parameter value (which describes the deviation of the surface temperature from that of a smooth surface in instantaneous equilibrium) of $\eta \leqslant 0.4$. This very low value is difficult to reconcile with the characteristics observed on real surfaces (J. R. Spencer 1990; E. Lellouch et al. 2013). In the study by E. Lellouch et al. (2017), Atacama Large Millimeter/submillimeter Array (ALMA) band 6 (1.3 mm) measurements of Makemake were used to determine the submillimeter emissivity. They obtained a relative emissivity of $\epsilon_r \approx 1$, in contrast to the $\epsilon_r \approx 0.7$ value typically observed on the surfaces of most Centaurs and trans-Neptunian objects. In the same paper, the authors explored two separate scenarios to model the thermal emission, incorporating the Spitzer/MIPS 24 μm measurement. One scenario involved a very dark satellite, while the other considered thermal emission from diffuse dust in instantaneous equilibrium with solar radiation. While technically both models could fit the observations to some acceptable level, they both had issues with the physical interpretation of the parameters obtained, and some open issues remained. (1) Is the mid-IR thermal emission excess observed at 24 μm during a single epoch a permanent feature? (2) Could further measurements of thermal emission provide additional constraints on the thermal properties? (3) Is it possible to discern which of the proposed models—dark terrain, dark satellite, or diffuse dust—is best suited to explain the observations?

To answer these key questions, we conducted a comprehensive investigation of the thermal emission of the Makemake system by integrating new measurements from the James Webb Space Telescope's (JWST) Mid-Infrared Instrument (MIRI), unpublished Herschel/PACS observations, and a reevaluation of previously published data. Additionally, we included visible light-curve data from the Transiting Exoplanet Survey Satellite (TESS) and Gaia space telescopes to constrain the rotation period and unpublished Spitzer/MIPS data at 24 and 70 μm from a second epoch, covering a substantial portion of Makemake's rotation period, to obtain a partial thermal light curve and constrain rotational thermal emission variations.

2. Observational Data and Thermal Emission Modeling

The details of the observations and data reduction are presented in Appendices A and B.

Visible-range light-curve measurements can provide rotational properties, which are essential for interpreting thermal emission data. We used data from the TESS and Gaia space telescopes. The light-curve measurements from both TESS and Gaia confirm the previously established 11.4 hr single-peaked rotation period obtained by T. A. Hromakina et al. (2019). The TESS double-peaked light curve (using a period of 22.8 hr) does not show a significant asymmetry between the light curves of the two half-periods; i.e., we cannot confirm that the double-peaked 22.8 hr is Makemake's true rotation period. In the following, we use $P = 11.4$ hr as the default rotation period, but in some cases we also perform calculations using $P = 22.8$ hr.

The thermal emission measurements of Makemake cover the wavelength range from 18 μm to 1.3 mm, observed by Spitzer/MIPS, Herschel/PACS and SPIRE, and ALMA; the latest measurements were performed with JWST/MIRI imaging in the F1800W and F2550W bands at 18.0 and 25.5 μm, respectively (see Tables 1 and 2 in Appendix B). These measurements are typically short snapshots, except for a longer Spitzer/MIPS 24 and 70 μm measurement sequence of 7.6 hr.

Although the Spitzer/MIPS 24 μm may indicate a small brightness variation ($\sim$16% peak-to-peak of the mean flux density level; see Appendix B), both the 24 and 70 μm long Spitzer/MIPS measurements are compatible with a constant light curve within $\lesssim$25% of the mean flux density level and are also compatible with the other 24 μm Spitzer measurements within this uncertainty. An obvious result from the thermal emission data is that the latest (2023 January) JWST/MIRI measurements confirm the previously seen high mid-IR flux densities at $\sim$25 μm and also show very high values, especially in the F1800W band (166 and 356 μJy at 18 and 25.5 μm, respectively). Thermal emission models of the Makemake system should be able to reproduce and explain the likely origin of these features.

To model the thermal emission of Makemake, we first used the NEATM (A. W. Harris 1998). Although this is a simple, compressed parameter model, its usage is justified, as we lack detailed information on Makemake's spin and shape properties, and we have only limited rotationally resolved thermal emission data. The NEATM concept uses the beaming parameter η as a proxy for thermal effects related to thermal inertia, surface roughness, spin rate, or subsolar latitude used in more complicated thermophysical models (J. R. Spencer 1990; E. Lellouch et al. 2013).

The NEATM model considers the observing geometry via the heliocentric distance of the target (r_h), the observer distance (Δ), and the phase angle (α). We transformed all observed flux densities to a common observing geometry of $r_h = 52$ au, $\Delta = 52$ au, and $\alpha = 1°$. We note, however, that the observing geometry changed only slightly between the different epochs, and the difference between the corrected and uncorrected flux densities is $\lesssim$4%, which is smaller than the relative uncertainties in the measured in-band flux densities ($\gtrsim$10%) and the additional $\sim$5% absolute calibration errors of the detectors. Submillimeter and millimeter data (Herschel/SPIRE and ALMA band 6) have been sourced from E. Lellouch et al. (2017). All other previously available IR data (Spitzer/MIPS and Herschel/PACS) have been reevaluated using the latest versions of the respective pipelines (see Appendix B). The 24 μm thermal light curve shows only a small amplitude variation, which may even correspond to a constant light curve, and we have no reliable light-curve information for the other wavelengths; however, multiepoch observations show similar values. Therefore, we used the weighted mean values per instrument/filter in our thermal emission modeling. These values were calculated from the data presented in Table 2.

We attempted to fit Makemake's thermal emission using three kinds of model configurations (see details in Appendix D). This approach involved accounting for the available size and albedo constraints for Makemake itself and also considering additional components. The models are (1) a single-terrain Makemake, (2) a single-terrain Makemake with a

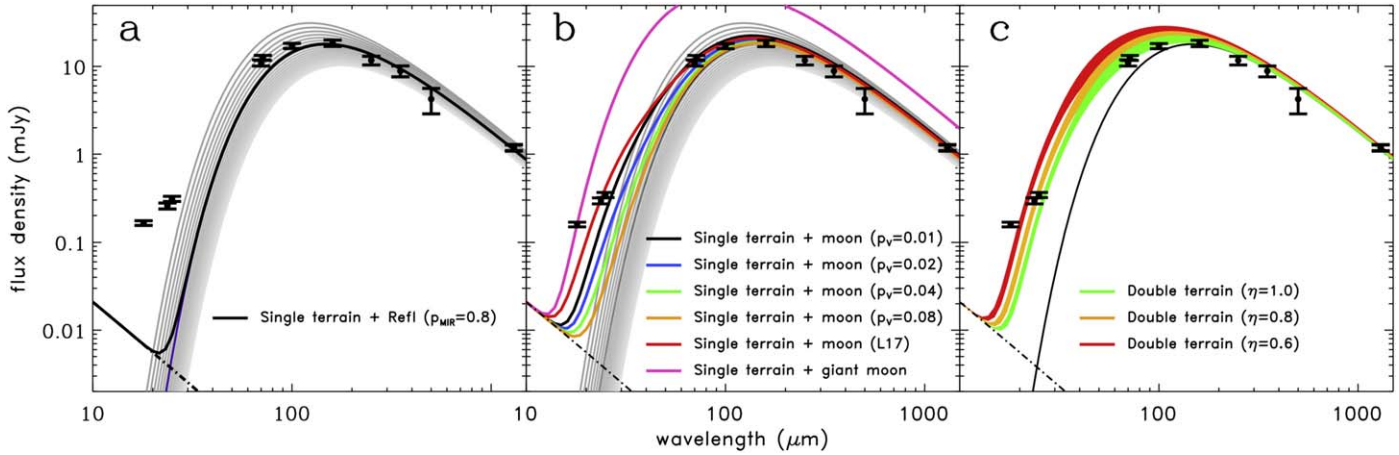

Figure 1. SED of Makemake from NEATM modeling. (a) Assuming a single terrain. Gray curves correspond to case 1 surfaces, assuming different η beaming parameters. The black solid curve has $\eta = 1.2$. The black dashed–dotted curve corresponds to a reflected-light contribution assuming a mid-IR albedo of $p_{\rm MIR} = 0.8$ in all subfigures. (b) Case 2: Makemake's thermal emission model considering a single-terrain Makemake and a dark satellite. The curves with different colors correspond to satellites with $p_V = 0.01$, ..., 0.08; the "extreme" moon model used by E. Lellouch et al. (2017; marked as L17); and the dark giant moon case, as indicated by the inserted text. (c) Makemake's thermal emission considering double-terrain models (case 3). The bands with different colors cover the models using different bright/dark terrains (see Table 3) and dark terrain locations but using the same beaming parameters, as shown by the colored symbols and extra text below the curves in the figures ("single terrain…", "double terrain…", etc.).

dark moon, and (3) a double-terrain Makemake featuring a mix of bright and dark areas. The results are presented in Figure 1. We note that reflected light has a nearly negligible contribution to our thermal measurements.

A single-terrain model (case 1; Figure 1(a)) can fit the long-wavelength part of the spectral energy distribution (SED) very well, indicating that the bright terrain component on Makemake is well described by this model. However, at $\lambda \leqslant 100\ \mu$m, the model deviates from the observed values, differing by 1–2 orders of magnitude.

Incorporating a dark satellite into the model (case 2; Figure 1(b)) improves the fit at shorter wavelengths and provides an acceptable fit at 70 μm. However, to fit the mid-IR flux densities, a very dark ($p_V \lesssim 0.02$) satellite with extreme thermal properties ($\eta = 0.34$) has to be considered, as suggested by E. Lellouch et al. (2017; labeled in the figure as L17). Even with this adjustment, the flux density measured by JWST/MIRI F1800W (18 μm) is still significantly underestimated by an order of magnitude. If a second—hypothetical—extremely large and dark satellite is added to the system, the 18 μm flux density can indeed be fitted ("giant moon"; magenta curve in Figure 1(b)). However, this additional body should have a diameter of ~1200 km, comparable to the size of Makemake, and a dark and rough terrain ($p_V = 0.04$, $\eta = 0.6$), which is clearly not supported by any measurements. Furthermore, in this scenario, the flux densities at all longer wavelengths are significantly overestimated, a result that is corroborated by thermophysical model calculations (see below).

Similarly, considering a mixture of bright and dark terrains (case 3; Figure 1(c)) can improve the fits at shorter wavelengths but cannot fit the mid-IR and far-IR observed flux densities at the same time, and the 18 μm flux density clearly requires additional surfaces, as in the case of the extra giant dark body above.

To confirm the validity of the previous NEATM calculations, we also performed thermophysical model calculations (J. S. V. Lagerros 1996, 1998) using a wide range of thermophysical model parameters (surface roughness, thermal inertia, spin properties) to obtain a radiometric size and albedo that match the observed flux densities. This showed, in agreement with the NEATM results, that while for the longer wavelengths, the occultation size is matched, a very large ($D = 4000$–6000 km equivalent size) and very dark ($p_V \leqslant 0.05$) Makemake (or another body) is needed to obtain the observed mid-IR flux densities, which is clearly incompatible with the observations.

As a conclusion, thermal emission of solid surfaces of airless bodies, heated by the solar irradiation alone, cannot fully reproduce the observed IR SED of Makemake. In particular, no model could fit the mid-IR excess seen by JWST/MIRI in the F1800W band.

A detailed analysis (Appendix C) also shows that neither reasonable contaminating sources (galaxy, bypassing main-belt asteroid) nor photometric color corrections or other instrument issues could feasibly explain the observed mid-IR flux densities. Therefore, the source of the mid-IR excess must be on or around Makemake. Below, we propose two possible scenarios to explain this very prominent mid-IR excess.

3. Makemake with a "Hot Spot"

Material from subsurface activity of icy bodies may reach the surface and cause excess temperatures. One prime example is Enceladus (J. R. Spencer et al. 2006), where Cassini detected 3–7 GW of thermal emission from the south polar troughs at temperatures up to at least 145 K from an equivalent area of ~350 km^2 (~10 km radius). We may assume that the origin of Makemake's mid-IR excess is similar.

In this scenario, we fitted the SED assuming a single-terrain Makemake and a "median" satellite contribution ($p_V = 0.04$), as described in Appendix D, and using a "hot spot" assuming that it has the SED of a single-temperature blackbody (Figure 2). For this additional component, we obtain a best-fitting blackbody temperature of $T_s = 147 \pm 5$ K, and the corresponding area has an equivalent radius of $r_s = 10.0 \pm 0.5$ km, i.e., ~0.02% of the apparent disk of Makemake. (Wright Mons on Pluto, a suspected cryovolcano, has a caldera of ~5 km in diameter; O. L. White et al. 2017; K. N. Singer et al. 2022). As the Spitzer/MIPS 24 μm flux densities show a small variation

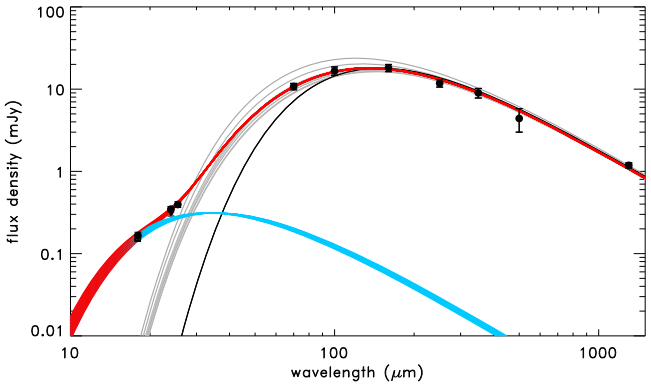

Figure 2. SED assuming an additional "hot spot" on the surface. Gray curves correspond to a single-terrain Makemake + a dark satellite with different albedos. The light blue curves correspond to blackbodies in the $T_s = 147 \pm 5$ K range. The red curves are the sum of the blue curves and the "median" Makemake + satellite curve, assuming a satellite with $p_{V,S} = 0.04$ and $D_s = 179$ km.

only ($\leqslant$20%; see Appendix B), in this scenario, the hot spot should be continuously visible and related to a continuously visible (polar) region. In this case, depending on the actual pole orientation, the actual true area may be significantly larger and still have an equivalent radius of $r_s = 10$ km due to projection effects. In the case of a perfectly equator-on configuration, a polar cap of $\sim 3\overset{\circ}{.}5$ radius in latitude would be required to produce the area and excess power observed, covering $\sim$1% of the total surface of Makemake. A 147 K blackbody corresponds to a radiated power surface density of $\sim$26 W m^{-2}, significantly larger than the typical $\lesssim$1 W m^{-2} on the other regions on Makemake's surface where the power output is determined by the solar irradiation. We can also calculate the total power radiated by this hot spot, assuming the two limiting cases. For an area with an equivalent radius of $r_s = 10.0 \pm 0.5$ km, the corresponding total power is $P_{\rm tot} = 8.3 \times 10^9$ W (coincidentally, quite similar to the values obtained for Enceladus), while it is 1.5×10^{11} W for the $3\overset{\circ}{.}5$ polar region assumed above. This can be compared with the 8×10^{11} W total power received by Makemake from the solar irradiation. With our current (lack of) knowledge about Makemake's surface, we cannot identify an obvious source that could be responsible for this high-temperature region.

However, C. R. Glein et al. (2024) suggested that the D/H ratio of Makemake observed by JWST (W. M. Grundy et al. 2024) is consistent with an abiotic and/or a thermogenic origin of methane. These processes require hydrated rocky cores with high interior temperatures of 420–670 K, which may have been reached early in Makemake's history, as supported by the available thermal evolution models. On such an internally evolved world, the origin of surface methane may be cryovolcanic outgassing from an interior water ocean or solid-state convection followed by clathrate degassing. Both processes can provide a substantial heat flow to the surface from the warm interior (W. M. Grundy et al. 2024). If the hot spot discussed here is the reason behind the mid-IR excess emission, then Makemake is only the fourth known solid planetary body—after Earth, Io, and Enceladus—that is sufficiently geologically active for its internal heat to be detected by remote sensing.

There are several scenarios that could potentially explain elevated surface temperatures. When trying to find some analogy with other active bodies with similar surface compositions, Triton has known surface activity in the form of plumes, which are usually explained as eruptive processes (see the summary by J. D. Hofgartner et al. 2022). Possible scenarios to explain this feature include versions of a solid-state greenhouse effect model where a layer of nitrogen ice is more transparent to the incident solar radiation than the emitted thermal radiation, leading to a temperature increase within or at the bottom of the ice layer. While in this particular model, N_2 is assumed, other ices, like CH_4, may play a similar role also on Makemake. However, the solid-state greenhouse effect can produce excess temperatures of $\lesssim$20 K only (R. H. Brown et al. 1990), and the observed $\sim$150 K associated with Makemake's mid-IR excess is notably above the melting temperatures of N_2 and CH_4 ices (63 K and 91 K, respectively), essentially ruling out this scenario.

Among classical cryomagmas, a solution of H_2O–NH_3–CH_3OH has the lowest freezing temperature of $\sim$150 K (see, e.g., J. S. Kargel 1998), very similar to the excess temperature observed for Makemake. However, the observed temperature may instead be a lower limit on the actual temperatures on warm fissures or flows if they are not a continuous sheet but are instead small-scale geologic features interspersed by cooler terrains. This effect is observed on Enceladus, where heat is localized along four "tiger stripes." If sources of anomalous thermal emission on Makemake exhibit similar behavior, then solutions with different solute concentrations, like water containing NH_3 or dissolved salts, would also be possible.

In light of the evidence for a geophysically active interior, as proposed by C. R. Glein et al. (2024) to explain methane formation, and the need to maintain methane on the surface against escape and photochemical/radiolytic loss processes (W. M. Grundy et al. 2024), cryovolcanism may support the scenario involving a subsurface water ocean rather than one dominated by solid-state convection (although see F. Nimmo & M. E. Brown 2023). Should the excess temperature be associated with cryovolcanism, observation of the variation of the excess temperature with time or rotational phase may provide more insights into the actual process.

Further insight into the plausibility of current geophysical activity can be elucidated by examining the energy balance. While the density of Makemake is currently uncertain (A. Parker et al. 2018), if we assume that it is composed of $\sim$70% rock and $\sim$30% water (like most Kuiper Belt objects; C. J. Bierson & F. Nimmo 2019), then we can estimate rock and water masses of $\sim 2.2 \times 10^{21}$ kg and $\sim 0.9 \times 10^{21}$ kg, respectively. For a radiogenic heating rate of 5.6 pW kg^{-1} of rock (S. J. Desch et al. 2009), we calculate $\sim$12 GW of current heat production in the interior. This is sufficient to explain our lower limit for the excess thermal emission (>8 GW). However, Makemake should also be releasing heat via thermal conduction spread over its surface. Thus, heat production is probably operating at a deficit, and Makemake would not be at a steady state if it was releasing such a large quantity of heat. The source of excess heat may reside in a subsurface water ocean that is now freezing. As an example, let us consider what the rate of heat release would be if a mass of liquid water comprising 1% of the total water inventory has been freezing over the past 10^6–10^7 yr. The amount of latent heat released is $\sim 3 \times 10^{24}$ J, which corresponds to $\sim$10–100 GW. This seems broadly consistent with the amount of heat needed to explain the thermal anomaly that we identified. Future modeling will

need to assess whether a subsurface ocean can persist until today, how liquids may be brought to the surface of Makemake, and why a burst of liquid water freezing happens to be taking place at the present time.

One important aspect of the cryovolcanic scenario is that this kind of activity may result in a significant amount of material that could potentially produce a global atmosphere. This has not been identified in occultation measurements, with an upper limit of 4–12 nbar surface pressure (J. L. Ortiz et al. 2012). At the current 52 au heliocentric distance, however, volatiles that may form Makemake's atmosphere, N_2 and/or CH_4, quickly recondense after being released and may just form a local atmosphere or plume around the active region (J. D. Hofgartner et al. 2019).

4. Dust around Makemake

One may also assume that the origin of the mid-IR excess is high-temperature dust made of small grains, as small grains tend to overheat due to their low emissivities, with the actual dust temperature depending on the composition and grain size (see, e.g., T. Henning & R. Stognienko 1996). These small grains may reach much higher temperatures than the ∼40 K equilibrium temperature at Makemake's heliocentric distance.

We perform dust temperature calculations for the case of Makemake in Appendix E. As we have seen above, temperatures around 150 K are required to explain the observed prominent mid-IR excess. Dust temperatures for a specific grain composition reach the maximum around a grain size of ∼100 nm, but temperatures around 150 K are reached for graphite or carbon grains only, indicating that likely carbonaceous composition and small grain sizes are required to be able to explain the mid-IR excess with diffuse dust.

Recent studies found ring systems around Centaurs and trans-Neptunian objects including Chariklo, Haumea, and Quaoar (F. Braga-Ribas et al. 2014; J. L. Ortiz et al. 2017; B. E. Morgado et al. 2023; C. L. Pereira et al. 2023), suggesting that these rings may be common around outer solar system bodies, and here we assume that diffuse dust around Makemake may have a similar form.

The chords of the 2011 April occultation (see Figure 2 in J. L. Ortiz et al. 2012) run through Makemake's limb roughly in the east–west direction, and an ellipsoidal fit provides an apparent ellipse with a position angle (long axis versus the north direction) of $9° \pm 24°$. As the orbit of Makemake's satellite is seen close to edge-on (A. Parker 2024, private communication), it is possible that there is a ring seen at a low opening angle ($B \lesssim 15°$, as allowed by the occultation chords) and with a position angle similar to that of the fitted ellipsoidal limb. This ring could have avoided discovery in the occultation measurements.

We performed radiative transfer model calculations using a simple ring model (Appendix F). Our results show that due to their lower dust temperatures, the SEDs of larger grains ($s \gtrsim$ 500 nm) cannot fit the observed mid-IR (18–25 μm) emission of Makemake. This is also the case for some of the small (100 or 200 nm) grains. If we use the respective SEDs normalized to the measured F1800W data, the SEDs of most materials overestimate the 24 and 25 μm data (e.g., olivine, pyroxene, water ice). On the other hand, the SEDs of 100–200 nm graphite grains considerably underestimate the observed 24 and 25 μm flux densities (i.e., these grains are "too hot"). Among the materials we investigate here, carbonaceous grains (V. G. Zubko et al. 1996) with grain sizes of 100–200 nm or graphite grains with grain sizes between 200 and 500 nm can fit all mid-IR data simultaneously (without violating the JWST/MIRI F560W detection of the reflected light), considering some possible contribution from other components (dark moon, dark terrain) in the system in addition to the cold and bright surface of Makemake.

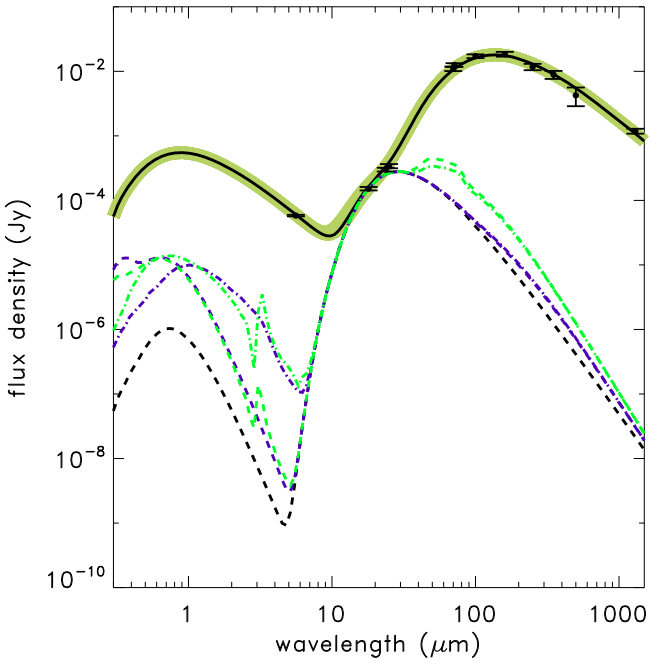

Figure 3. SED of Makemake's reflected light and thermal emission. Black symbols represent the mean measured flux densities. The green stripe shows the SED of the "hot-spot" models, compatible with the observations, as described in Section 3 (note that the stripe was made somewhat wider than it is in reality for better visibility). It was calculated assuming that Makemake has a double terrain with "Quaoar-like" dark terrains and reflected light with a mid-IR albedo of $p_{5.6} = 0.8$. The black dashed curve is the SED of 100 nm carbonaceous grains that together with Makemake's contribution (solid black curve inside the green stripe) matches the observed flux densities very well. The colored dashed/dashed–dotted curves correspond to the emission of dust when other types of dust grains are also included, in addition to the same amount of 100 nm carbonaceous dust as in the pure case. The additional material has a mass of 100× the mass of 100 nm carbonaceous grains in all cases. The additional components are as follows: purple dashed curve, pyroxene with 100% Mg content, 100 nm grain size; purple dashed–dotted curve, pyroxene with 100% Mg content, 1 μm grain size; green dashed curve, amorphous water ice, 100 nm grain size; green dashed–dotted curve, amorphous water ice, 1 μm grain size.

In Figure 3, we present the SED of Makemake with a ring made of 100 nm sized carbonaceous grains (black solid curve), with an additional contribution of a double-terrain model using Quaoar-like secondary terrain (see Appendix D); however, using a dark satellite model instead of double terrain provides very similar results. This particular model gives a very good match to the observed flux densities and is practically indistinguishable from the best-fit "hot-spot" model (Section 3 and green stripe in Figure 3). If the ring was made exclusively of these very small grains, the optical depth of the ring in the visible range would be $\tau \approx 0.1$, assuming a thin and narrow disk, a ring width of 10 km, and a ring radius of $r = 4300$ km, corresponding to the 3:1 spin–orbit resonance, similar to those found around other small bodies (F. Braga-Ribas et al. 2014; J. L. Ortiz et al. 2017; B. E. Morgado et al. 2023). Note that the optical depth depends on the actual ring width chosen and is smaller for a wider ring.

All known dusty rings of the giant planets are associated with denser rings or small moons, which also serve as dust sources via micrometeorite impacts, resupplying the small grains in the ring, which are quickly lost from the system due to nongravitational effects (M. M. Hedman et al. 2018). If Makemake's dusty ring exists, it is likely that it contains material with a wider range of grain sizes and may be a mixture of compositions. Using a few simple examples, we tested how the presence of other materials would modify the SED of the ring. Due to the predominantly cold temperatures of Makemake's surface (∼40 K), larger grains, which have similarly low dust temperatures, do not contribute notably to the mid-IR emission, and they have to "compete" with Makemake's cold thermal emission to be visible in the far-IR. This is also true for the large ($\gtrsim$100 μm) particles that make up the classical giant planet rings. In Figure 3, we present a few examples in which we added the contribution of different grains to that of 100 nm carbonaceous grains. The contribution of the additional material is 100 times the mass of the 100 nm carbonaceous grains in all cases. In all these cases, the mid-IR emission remains dominated by the 100 nm carbonaceous grains, with a negligible contribution from the other materials. While these additional materials dominate the reflected light and, in some cases, the far-IR emission of the ring, they do not change the overall SED due to the dominance of the reflected light and thermal emission from Makemake itself. One important aspect is, however, that adding these materials pushes the visible-range opacities to $p \lesssim 1$, which makes the ring easily detectable by stellar occultations, when the chords are cutting through these structures.

Small grains will be strongly affected by solar radiation through radiation pressure and Poynting–Robertson effects (J. A. Burns et al. 1979). We performed a detailed calculation of the particle lifetime (see Appendix G) using a dynamical model considering solar radiation pressure effects and assuming that the grains start orbiting Makemake in circular orbits. We estimate that the lifetime of the smallest carbonaceous grains—which are suspected to be responsible for the mid-IR excess emission—is ∼10 yr, depending on the starting semimajor axis (see Figure 11 in Appendix G). We note, however, that a small shepherding moonlet may help to stabilize the orbits of the ring particles and significantly extend the lifetime of the grains, like has been proposed in the case of Chariklo (H. Salo & B. Sicardy 2024; A. A. Sickafoose & M. C. Lewis 2024). All other timescales, including the collisional timescale of dust grains and the decay due to the Poynting–Robertson drag (J. A. Burns et al. 1979; C. D. Murray & S. F. Dermott 1999), are orders of magnitude longer than the radiation pressure timescale for small grains and likely do not play an important role here.

The ring proposed to explain Makemake's mid-IR excess here would be a new type of ring in the Centaur and trans-Neptunian regions. The thermal emission of the Haumea, Chariklo, or Quaoar rings does not show a similar strong mid-IR excess emission (E. Lellouch et al. 2017; T. Müller et al. 2019; C. Kiss et al. 2024); however, recent results from stellar occultations suggest that very small grains may dominate some small-body rings in the outer solar system (P. Santos-Sanz et al. 2024, private communication). While the "classical" rings of Saturn and Uranus are known to be mostly millimeter-to-centimeter-sized grains or pebbles (J. N. Cuzzi et al. 2018; P. D. Nicholson et al. 2018), the thermal emission of the Phoebe ring around Saturn (A. J. Verbiscer et al. 2009) is dominated by small grains, and it is characterized by a very steep size distribution law, as obtained by Wide-field Infrared Survey Explorer and Spitzer measurements (size distribution power-law index of $q = 4$–6; D. P. Hamilton et al. 2015). In the case of the Phoebe ring, dust particles originated from the satellite Phoebe itself from micrometeorite or larger impacts and are thought to be responsible for the dark material on the leading hemisphere of Iapetus (D. Tamayo et al. 2011). Similarly, an additional small inner satellite may be responsible for the ring material in the case of Makemake. As the lifetime of the small grains in the putative Makemake ring is on the order of a decade, in the case of a single event, a fading should have been observed in the last ∼20 yr, covered by mid-IR observations. However, the earlier Spitzer/MIPS and the recent JWST/MIRI data show compatible flux densities, indicating that there may be a continuous replenishment of dust that keeps the ring material continually observable. Concerning the composition of dust grains, carbon is ubiquitous in the outer solar system. Submicron cometary dust is dominated by amorphous carbon (D. E. Harker et al. 2023), and, as we have shown above, due to their unique optical properties, very small carbonaceous dust grains may be the dominant source of the mid-IR thermal emission even in the presence of other types of grains. Using our radiative transfer calculations, we estimate that, assuming solely 100 nm carbonaceous grains, the total mass of the ring is $\sim 3 \times 10^6$ kg, equivalent to the mass of a body with a ∼10 m radius. This is likely a lower limit, as larger grains may contribute significantly without notably modifying the SED of the system, as was shown above. Assuming the presence of larger grains with 100 times the mass of small grains, the mass of the ring could be $3 \times 10^6\,\mathrm{kg} \lesssim M_r \lesssim 3 \times 10^8$ kg. With the short lifetime of ∼10 yr of the very small grains, a rate of $\dot{M}_r \gtrsim 3 \times 10^5\,\mathrm{kg\,yr^{-1}}$ is required for replenishment, and probably a higher amount considering the whole scale of particle sizes that may originate from small moons or collisions between large ring particles.

5. Conclusions

We have shown that the trans-Neptunian dwarf planet (136472) Makemake exhibits a prominent mid-IR excess that cannot be explained by the thermal emission of solid bodies irradiated only by the Sun at the heliocentric distance of Makemake.

We proposed two separate scenarios to explain this mid-IR excess: a hot spot powered by cryovolcanism or a ring made of very small carbonaceous grains. Interestingly, these two phenomena may be interconnected. The material of Saturn's E ring originates from Enceladus's water geysers (see, e.g., M. M. Hedman et al. 2018 for a summary), and similar processes may supply material to a ring around Makemake. In addition, Saturn's E ring is also dominated by submicron-sized grains. If these processes can put small carbonaceous or graphite grains around Makemake (e.g., in addition to water-ice grains), the actual observed IR excess may be a result of a combination of the two phenomena.

The Spitzer/MIPS partial light curve (Appendix B) indicated a small amplitude (16%) variation at 24 μm; however, a flat light curve could not be excluded. Additional mid-IR (10–25 μm) measurements sampling Makemake's thermal emission at multiple subobserver longitudes may confirm this rotational variation, which could be a strong indication that the excess emission at least partly comes from Makemake's

surface. However, a rotationally constant excess emission does not automatically prove the existence of a ring. Additional mid-IR observations may also show whether the excess—both the intensity and the associated temperature—has changed since the latest JWST/MIRI measurements in 2023 January. This is expected in the ring scenario if the responsible small dust grains were created in a single event. However, in the case of a hot spot, the excess may also change due to changes in the underlying processes (e.g., cooling cryolava). Future occultation measurements may indeed help to solve the ring-versus-hot-spot puzzle.

Acknowledgments

The research leading to these results has received funding from the K-138962 and TKP2021-NKTA-64 grants of the National Research, Development and Innovation Office (NKFIH, Hungary). P.S.-S. acknowledges financial support from the Spanish I+D+i project PID2022-139555NB-I00 (TNO-JWST) funded by MCIN/AEI/10.13039/501100011033. P.S.-S. and J.L.O. acknowledge financial support from the Severo Ochoa grant CEX2021-001131-S funded by MCIN/AEI/10.13039/501100011033. C.R.G. was supported by the NASA Astrobiology Institute through its JPL-led team entitled Habitability of Hydrocarbon Worlds: Titan and Beyond. This work is based in part on observations made with the NASA/ESA/CSA James Webb Space Telescope. The data were obtained from the Mikulski Archive for Space Telescopes at the Space Telescope Science Institute, which is operated by the Association of Universities for Research in Astronomy, Inc., under NASA contract NAS 5-03127 for JWST. We thank our reviewer for the comments and corrections.

Facilities: TESS (G. R. Ricker et al. 2015), JWST/MIRI (G. S. Wright et al. 2023), Spitzer/MIPS (G. H. Rieke et al. 2004), Herschel/PACS (A. Poglitsch et al. 2010).

Software: FITSH (A. Pál 2012), OPTOOL (C. Dominik et al. 2021), RADMC-3D (C. P. Dullemond et al. 2012).

Appendix A
Visible-range Light Curves

TESS data. TESS (G. R. Ricker et al. 2015) observed Makemake in Sector 23 between 2020 March 19 and April 15 and in Sector 50 between 2022 March 26 and April 22. The Sector 50 data are heavily affected by stray light; therefore, we used the Sector 23 measurements only. Basic data reduction was performed with the TESS reduction pipeline developed for solar system targets, as described in A. Pál et al. (2020). Due to the large pixel size of 21″ and the slow motion of Makemake in the sky, the photometry is affected by the relative position of the measuring aperture and the edge of the actual pixel, introducing characteristic frequencies in the residual spectrum related to the *X*- and *Y*-direction of motion of the target through the field of view. To account for this effect, we used the measured brightness values of Makemake versus the *X* and *Y* pixel fractions and produced phase dispersion spectra in a way similar to that of the "normal" light curve (brightness versus time; see Figure 4). The *X* and *Y* residual spectra show prominent frequencies at $f \approx 3\ \mathrm{c\ day^{-1}}$ and $f \leqslant 0.3\ \mathrm{c\ day^{-1}}$, respectively, corresponding to the apparent motion and pixel-crossing times of Makemake in the specific directions. One of the prominent peaks in the residual spectrum apart from the *X* and *Y* motion frequencies is at $f = 2.105 \pm 0.014\ \mathrm{c\ day^{-1}}$

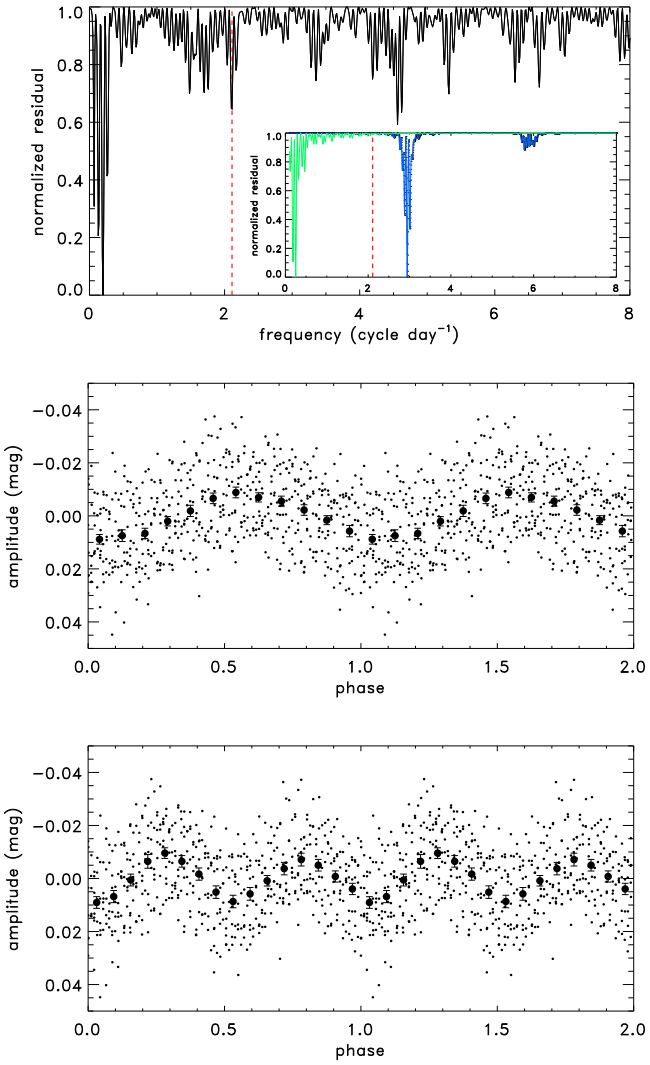

Figure 4. Top: phase dispersion vs. frequency of the Makemake TESS data. The inset shows the residual spectrum derived using the position of the aperture centers with respect to the actual pixel's edge in the *X* (blue) and *Y* (green) directions. In both the main figure and the inset, the vertical dashed red line is at the frequency of $f = 2.105\ \mathrm{c\ day^{-1}}$ ($P = 11.401$ hr) associated with the prominent peak in the residual spectrum, very close to the 11.41 hr period identified by T. A. Hromakina et al. (2019). Middle: light curve folded with a period of $P = 11.401$ hr. Black dots represent the binned data. Bottom: light curve folded with the double period, $P = 22.802$ hr.

($P = 11.401 \pm 0.076$ hr), very close to the single-peak solution obtained by T. A. Hromakina et al. (2019). After correcting for the effect of the *X* and *Y* motion contribution, we obtained the light curve folded by this $f = 2.105\ \mathrm{c\ day^{-1}}$ frequency as presented in Figure 4, showing a peak-to-peak amplitude of $\Delta m = 0.018 \pm 0.002$ mag, notably smaller than the previous $\Delta m = 0.032 \pm 0.005$ mag amplitude obtained by T. A. Hromakina et al. (2019). We also investigated whether a single- or double-peaked light curve is preferred, in the latter case using the double period, $P = 22.8$ hr. Comparing the first and second half-periods of the double-peaked folded light curve using the method in A. Pál et al. (2016) and also applying a Student's *t*-test (see T. A. Hromakina et al. 2019), both methods agree that the two half-periods are different at the $\sim 1.7\sigma$ level; i.e., we cannot unambiguously distinguish between single- and double-peaked light curves.

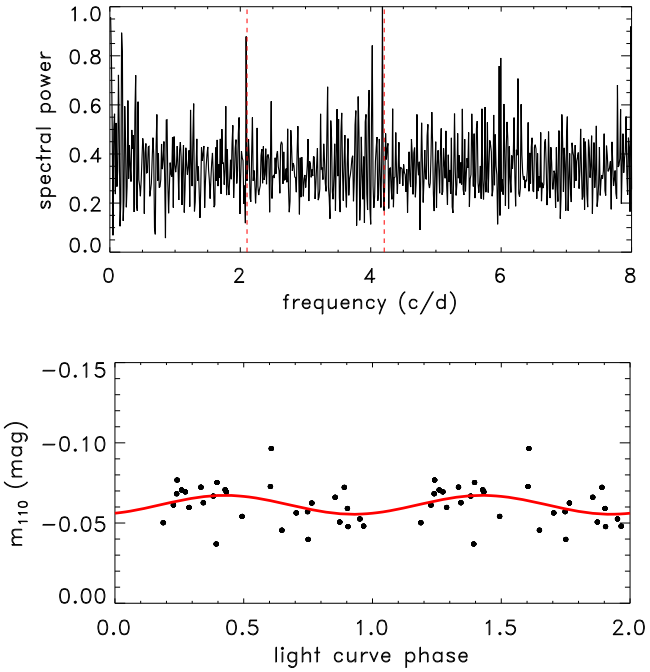

Figure 5. Top: Lomb–Scargle periodogram of the Makemake Gaia data. The vertical dashed lines mark the frequency corresponding to the 11.41 hr period, identified by T. A. Hromakina et al. (2019), and the first overtone at 5.7 hr. Bottom: heliocentric and observer-distance- and phase-angle-corrected Gaia light curve, folded with the $P = 11.4767$ hr period.

Gaia data. Gaia data of Makemake are available in the third Gaia Data Release (Gaia Collaboration et al. 2023), accessible in the Gaia Science Archive[16] through the *gaiadr3.sso_observation* table. The table contains data obtained during the transit of the source on a single CCD during a single transit. For Makemake, the typical photometric errors of the individual data points are ∼0.4% of the flux density. More details about the Solar System Objects in the Gaia DR3 are discussed in P. Tanga et al. (2023). Gaia *G*-band data of Makemake were corrected for heliocentric and observer distance and phase angle using spacecraft-centric data obtained from the NASA Horizons system (J. D. Giorgini et al. 1996). We applied a linear phase angle correction using the heliocentric and observer-distance-corrected brightness values, and we used these reduced magnitudes for the period search. We applied both a residual minimization method (see, e.g., A. Pál et al. 2015) and a Lomb–Scargle periodogram algorithm, which resulted in essentially the same results.

The Lomb–Scargle periodogram is presented in Figure 5 and shows two primary peaks, one at $f = 2.0912 \pm 0.0015$ c day^{-1}, or $P = 11.4767 \pm 0.0082$ hr, and another peak at its first overtone at $f = 4.1793 \pm 0.0033$ c day^{-1}, or $P = 5.7425 \pm 0.0045$ hr, with a peak-to-peak amplitude of $\Delta m = 0.012 \pm 0.002$ mag. Both peaks have a signal-to-noise ratio of ≈3 over the general spectral power fluctuation level, around the acceptable level of significance. The $P = 11.4767$ hr period is very close to the 11.41 hr single-peak period identified by T. A. Hromakina et al. (2019) and also by us (11.40 hr) in the TESS data. The $\Delta m = 0.012 \pm 0.02$ mag Gaia amplitude is lower than the $\Delta m = 0.018 \pm 0.002$ mag obtained from the TESS data and significantly lower than the $\Delta m = 0.032$ mag reported by T. A. Hromakina et al. (2019).

Some difference between the light-curve amplitudes may be explained by the different filter transmission curves; i.e., the Gaia *G*-band filter is very wide and covers the spectral range between ∼400 and 900 nm, while TESS sensitivity is mostly confined to the 600–1000 nm range. Also, as Makemake orbits the Sun, the aspect angle of the spin axis changes; therefore, the light-curve amplitude changes as well. The T. A. Hromakina et al. (2019) study mixes observations with different instruments/filters from a wider period, including measurements from 2009 to 2017. This is a long time span, and consequently, observations may include light curves with different amplitudes at different times—this may at least partially explain the different half-periods in the case of a double-peaked light curve, leading the double-peaked light curve to be their preferred solution. Due to the low number of data points and the sporadic nature of the data, Gaia measurements could not be used to distinguish between single- and double-peaked light curves.

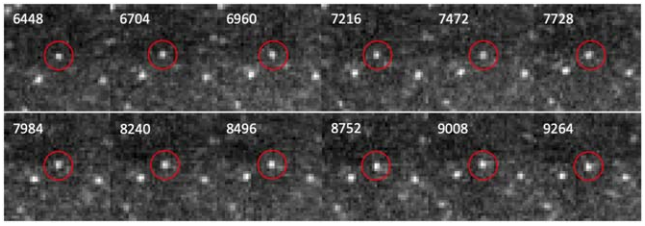

Figure 6. Spitzer/MIPS 24 μm images of Makemake, with AORKEYs 19176448–19179264 (see Table 1 for the flux densities derived).

Appendix B
IR Observations and Data Reduction

MIPS 24/70 μm measurements and 24 μm partial light curve. Makemake was observed with MIPS of the Spitzer Space Telescope (G. H. Rieke et al. 2004) at two epochs, on 2005 June 20/21 and on 2007 June 5 (see also Table 1). The first epoch measurement consisted of two AORKEYs covering 0.82 hr, while the second epoch covered 7.6 hr with 12 AORKEYs, in both cases using both the 24 and 70 μm cameras. In the case of the 24 μm maps, we used the calibrated, post basic calibrated data (BCD) MAIC maps. The block of measurements made during the second epoch consists of 12 AORKEYs and altogether lasted ∼7.6 hr, covering a significant fraction of a full rotation, assuming the 11.4 hr period discussed above. At 24 μm, the source was clearly identified and bright with respect to the background in all individual Astronomical Observation Request (AOR) images. The sequence of images (Figure 6) clearly shows Makemake moving through the field and indicates faint sources in the background that may notably affect the photometry. To account for this effect, we performed a background subtraction by dividing the 12 frames into two six-frame groups. We produced two "shadow" images, the first one (S1) being the average image of the first two frames, and the second one (S2) being the average image of the last two frames. We used S2 to correct for the background of the first six frames and S1 to correct for the background of the last six frames. Still, as Makemake moved ∼14″ during the whole measurement, the distance between the closest frame and the corresponding shadow images is just ∼8″, only slightly larger

[16] https://gea.esac.esa.int/archive/

Table 1
Summary of Thermal Emission Observations of Makemake, Including Herschel/PACS and SPIRE, Spitzer/MIPS, and ALMA Observations

ObsID/AORKEY	Instrument	JD_{start}	JD_{end}	t_{tot} (hr)	r_h (au)	Δ (au)	α (deg)	λ (deg)	β (deg)	Bands (μm)
				Herschel						
1342187319	SPIRE	2455165.45072	2455165.46387	0.316	52.138	52.409	1.051	176.544	28.705	250, 350, 500
1342187320	SPIRE	2455165.46453	2455165.47767	0.316	52.138	52.409	1.051	176.544	28.705	250, 350, 500
1342187366	PACS	2455166.28238	2455166.30072	0.440	52.138	52.397	1.055	176.552	28.712	70, 160
1342187367	PACS	2455166.30156	2455166.31990	0.440	52.138	52.397	1.055	176.552	28.712	100, 160
1342187524	SPIRE	2455167.26799	2455167.28113	0.316	52.138	52.383	1.059	176.561	28.720	250, 350, 500
1342187525	SPIRE	2455167.28179	2455167.29494	0.316	52.138	52.383	1.059	176.561	28.720	250, 350, 500
1342197657	PACS	2455350.40924	2455350.41907	0.236	52.165	51.959	1.104	174.615	28.976	70, 160
1342197658	PACS	2455350.41980	2455350.42964	0.236	52.165	51.959	1.104	174.615	28.975	70, 160
1342197659	PACS	2455350.43037	2455350.44021	0.236	52.165	51.959	1.104	174.615	28.975	100, 160
1342197660	PACS	2455350.44094	2455350.45078	0.236	52.165	51.959	1.104	174.615	28.975	100, 160
1342197695	PACS	2455351.22786	2455351.23770	0.236	52.165	51.971	1.107	174.613	28.968	70, 160
1342197696	PACS	2455351.23843	2455351.24826	0.236	52.165	51.971	1.107	174.613	28.968	70, 160
1342197697	PACS	2455351.24899	2455351.25883	0.236	52.165	51.971	1.107	174.613	28.968	100, 160
1342197698	PACS	2455351.25956	2455351.26940	0.236	52.165	51.971	1.107	174.613	28.968	100, 160
1342198251	SPIRE	2455360.70866	2455360.73309	0.586	52.166	52.111	1.126	174.612	28.882	250, 350, 500
1342198451	SPIRE	2455358.09508	2455358.11951	0.586	52.166	52.072	1.123	174.609	28.906	250, 350, 500
				Spitzer						
13803776	MIPS	2453542.19492	2453542.21199	0.410	51.883	51.869	1.122	169.577	29.026	24, 71.42
13803264	MIPS	2453543.42211	2453543.43920	0.410	51.884	51.887	1.122	169.580	29.014	24, 71.42
19179264	MIPS	2454256.98375	2454257.01009	0.632	52.001	51.523	0.984	171.788	29.281	24, 71.42
19179008	MIPS	2454257.01442	2454257.04076	0.632	52.001	51.523	0.984	171.787	29.281	24, 71.42
19178752	MIPS	2454257.04507	2454257.07141	0.632	52.001	51.524	0.984	171.787	29.281	24, 71.42
19178496	MIPS	2454257.07573	2454257.10207	0.632	52.001	51.524	0.985	171.787	29.280	24, 71.42
19178240	MIPS	2454257.11113	2454257.13748	0.632	52.001	51.525	0.985	171.786	29.280	24, 71.42
19177984	MIPS	2454257.14178	2454257.16813	0.632	52.001	51.525	0.985	171.786	29.280	24, 71.42
19177728	MIPS	2454257.17244	2454257.19878	0.632	52.001	51.525	0.985	171.786	29.280	24, 71.42
19177472	MIPS	2454257.20309	2454257.22946	0.633	52.001	51.526	0.985	171.785	29.279	24, 71.42
19177216	MIPS	2454257.24230	2454257.26867	0.633	52.001	51.526	0.986	171.785	29.279	24, 71.42
19176960	MIPS	2454257.27676	2454257.30310	0.632	52.001	51.527	0.986	171.785	29.279	24, 71.42
19176704	MIPS	2454257.30743	2454257.33377	0.632	52.001	51.527	0.986	171.785	29.279	24, 71.42
19176448	MIPS	2454257.33807	2454257.36441	0.632	52.001	51.527	0.987	171.784	29.278	24, 71.42
				ALMA						
	ALMA	2457449.78750	2457449.80278	0.311	52.439	51.622	0.620	182.249	28.945	1300

Note. The columns list the observation ID (AORKEY/ObsID), instrument, start and end times in Julian Date, target heliocentric distance, observer-to-target distance, phase angle, and central wavelengths of the filters/bands used.

than the $\sim 6''$ FWHM of the MIPS 24 μm point-spread function (PSF).

This means that when the shadow images are subtracted, the "mirror image" of Makemake will still affect the photometry on the background-subtracted images, notably decreasing the measured flux density. We simulated this effect by using the MIPS 24 μm PSF and subtracted equal-brightness sources at different distances from the target source. Using a small aperture with a radius of 3 pixels ($\sim 7''$), the background subtraction has a very small effect at the largest, $\sim 14''$, distances, and we obtain $\geqslant 99\%$ of the true flux density; at the small distances ($\sim 8''$), however, we obtain $\sim 60\%$ only. These simulated flux density ratios can be used to correct the measured background-subtracted flux densities.

To check the possible flux density variations, we used these simulated mirror source distance-dependent flux density corrections, also allowing for a sinusoidal 24 μm light-curve variation with a fixed period of $P = 11.4$ hr, and we searched for the best-fit mean flux, amplitude, and phase by residual minimization. The results are presented in Figure 7. The observed 24 μm light curve can be best fit by a low-amplitude sinusoidal light curve with a relative peak-to-peak amplitude of $16\% \pm 3\%$ or $\Delta F_{24} = 0.047 \pm 0.009$ mJy, over the $F_{24}^0 = 0.295 \pm 0.025$ mJy mean in-band flux density. However, this light curve is also compatible with a constant light curve with 0.08 mJy uncertainty ($\sim 25\%$ of the mean value). We note that due to the uncertainties in the period determination, the visible-range light curves cannot be phased to the thermal emission measurements, as they are separated by several years.

At 70 μm, we cannot perform the same background subtraction as for the 24 μm images due to the larger FWHM of the PSF ($\sim 18''$); i.e., the 70 μm images may still contain contamination from background sources. We performed aperture photometry using an aperture radius of $8''$ and a background annulus between $39''$ and $65''$ on the pipeline-processed (post-BCD) filtered (MFILT) images, downloaded from the Spitzer Heritage Archive. We obtained a mean in-band flux density of $F_{71} = 11.17 \pm 0.50$ mJy for the AORKEYs 19176448...19179264, and the observed 70 μm light

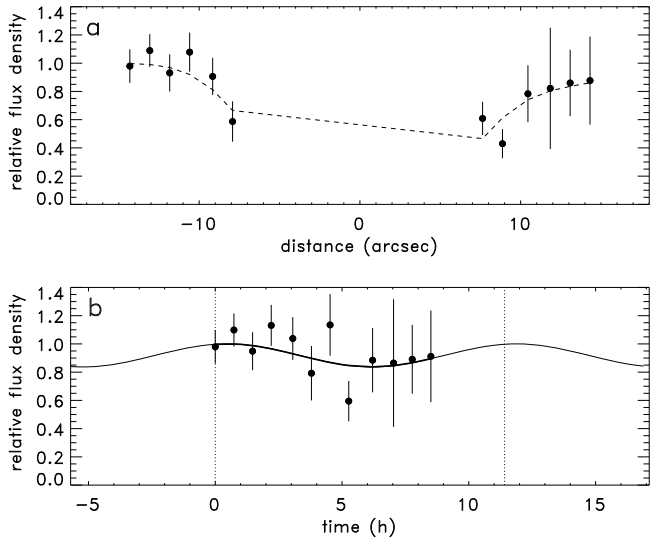

Figure 7. (a) Relative flux densities as measured in the background-subtracted MIPS 24 μm images as a function of relative distance between the target and the mirror source. Negative and positive distances correspond to the first and second half of the measurement, respectively. The dashed curve represents the best-fit theoretical background-corrected relative flux density curve, considering flux loss due to the subtraction of the "mirror" source and assuming a sinusoidal variation with a period of $P = 11.41$ hr. (b) Variation of relative flux densities as a function of time (black dots) using the same best-fit sinusoidal fit as above (solid curve). The thicker part of the curve represents the phases covered by the MIPS 24 μm observations.

curve is compatible with a constant light curve with a ± 2.93 mJy uncertainty (25% of the mean value).

The same basic reduction steps were applied for the other measurement pair (AORKEYs 13803776/3264) without background subtraction (see Tables 1 and 2). The flux densities obtained in these cases are compatible with the average in-band flux densities obtained by J. Stansberry et al. (2008): $F_{24} = 0.30 \pm 0.02$ mJy and $F_{71} = 14.6 \pm 2.2$ mJy.

Herschel Space Observatory measurements. Makemake was observed with the PACS photometer in chop–nod mode in the SDP (T. L. Lim et al. 2010). Note that this mode was used for faint source photometry early in the mission and was replaced by the recommended (mini) scan map mode after the SDP (M. Nielbock et al. 2013; C. Kiss et al. 2014). Sources observed in chop–nod mode could have serious contamination by background sources, as the final background of the image was made undecryptable by multiply folding the original "chopped" and "nodded" subimages. T. L. Lim et al. (2010) obtained 11.4 ± 2.7, 12.0 ± 2.8, and 16.7 ± 3.5 mJy at 70, 100, and 160 μm. We reevaluated this data set, consisting of 70/160 μm and 100/160 μm filter combination measurements. We used the latest Herschel Science Archive Standard Product Generation level 2 high-pass-filtered images and performed the photometry in HIPE (version 15.0.0). We used the *annularSkyAperturePhotometry()* task and the recommended apertures of 12″, 12″, and 20″ radii (M. Nielbock et al. 2013) in the three bands, respectively, to obtain the flux densities, and we used *photApertureCorrectionPointSource()* to perform the encircled energy fraction correction (Z. Balog et al. 2014). Flux density uncertainties are obtained using a set of circular apertures placed at a distance of 20″ at 70 and 100 μm and 28″ at 160 μm (see, e.g., U. Klaas et al. 2018). The flux densities obtained are 12.06 ± 1.54, 13.84 ± 1.53, and 16.91 ± 1.57 mJy at 70, 100, and 160 μm (also listed in Table 2). These flux density values are somewhat larger than those obtained by T. L. Lim et al. (2010) at 70 and 100 μm and very similar at 160 μm.

Makemake was also observed in scan map mode, in the framework of the "TNOs are Cool!" Open Time Key Program (T. G. Müller et al. 2009). The measurements followed the standard "TNOs are Cool!" measurement sequence; i.e., the target was observed at two epochs (referred to as Visit-1 and Visit-2), and the time between the two visits was set in a way that the target moved ∼30″ with respect to the sky background, which allowed us to use observations at the two epochs as mutual backgrounds. Observations at a specific visit also included scan/cross-scan observations in the same band and in both possible PACS photometer filter combinations (70/160 and 100/160 μm; see Table 1). Data reduction of the data is performed with the faint moving target optimized version of the PACS reduction pipeline (C. Kiss et al. 2014) that produces level 2 high-pass-filtered maps from the individual scan map observations (ObsIDs). The scan and cross-scan images of the PACS band are combined to produce the "coadded" images for each epoch. The coadded images of the two epochs are further combined to obtain background-eliminated differential (DIFF) images. The "background matching" method of C. Kiss et al. (2014) is applied to correct for the small offsets in the coordinate frames of the Visit-1 and Visit-2 images using images of systematically shifted coordinate frames and then determining the offset that provides the smallest standard deviation of the per-pixel flux distribution in a predefined coverage interval—the optimal offset can be most readily determined using the 160 μm images due to the strong sky background with respect to the instrument noise. The DIFF images contain a "positive" and a "negative" source separated by ∼30″, corresponding to the two observational epochs. While higher-level data products also exist (e.g double-DIFF images; see C. Kiss et al. 2014), in this paper, we used the DIFF images to obtain photometry separately at the two epochs. Flux densities are obtained using the faint source optimized "TNOs are Cool!" photometry pipeline, including the derivation of the flux density uncertainties using the implanted source method (C. Kiss et al. 2014). The results are presented in Table 2.

The Herschel/SPIRE submillimeter photometer also observed Makemake; the latest reevaluation of the results is available in E. Lellouch et al. (2017). The monochromatic flux densities obtained are 12.5 ± 1.3 mJy, 9.5 ± 1.3 mJy, and 4.7 ± 1.5 mJy at 250, 350, and 500 μm, respectively, from multiepoch observations. We used these combined flux densities in our subsequent analysis.

JWST MIRI imaging observations. Makemake was observed in the framework of the Guaranteed Time Observations program 1254 "TNOs" (PI: A. Parker) in the F1800W and F2550W bands of the MIRI imaging instrument (G. H. Rieke et al. 2015) of the JWST. The JWST data presented in this Letter were obtained from the Mikulski Archive for Space Telescopes (MAST) at the Space Telescope Science Institute.[17] To ensure the most up-to-date calibration, the raw *uncal* files were downloaded from MAST and processed locally using version 1.15.1 of the JWST calibration pipeline (H. Bushouse et al. 2024) and the *jwst_1256.pmap* reference file context. None of the default pipeline parameters were changed when processing the science, background, or target acquisition observations. The fully calibrated, non-distortion-corrected *cal* files were used in this

[17] The specific observations analyzed can be accessed via doi:10.17909/0ebf-dp91.

Table 2
Far-IR and Submillimeter Observations of Makemake

Instrument/Mode	ObsID/AORKEY	t_{exp} (hr)	JD_{mid}	Band (μm)	F^i (mJy)	Data Product	References
			JWST				
MIRI	V01254001001P0000000003101	0.14	2459975.0067	18.0	0.169 ± 0.008		This work
	V01254002001P0000000003101	0.14	2459975.0146	18.0	0.167 ± 0.008		
	V01254001001P0000000003103	0.14	2459975.0242	25.5	0.361 ± 0.023		
	V01254002001P0000000003103	0.14	2459975.0323	25.5	0.352 ± 0.022		
	V01254001001P0000000002101	0.003	2459975.07637	5.6	0.058 ± 0.003	TAQ image	
			Herschel				
SPIRE	1342187319,320,524,525 1342198251,451	2.44	2455261.7851	250	11.8 ± 1.2		L17
SPIRE	1342187319,320,524,525 1342198251,451	2.44	2455261.7851	350	9.0 ± 1.2		L17
SPIRE	1342187319,320,524,525 1342198251,451	2.44	2455261.7851	500	4.4 ± 1.4		L17
PACS	1342187366	0.44	2455166.2915	70	12.06 ± 1.54	SPG/HPF	This work
Chop–nod	1342187367	0.44	2455166.3107	100	13.84 ± 1.53		
	1342187366-367	0.88	2455166.3011	160	16.91 ± 1.57		
PACS	1342197657-7658	0.98	2455350.4194	70	11.57 ± 1.08	DIFF1	This work
Scan maps	1342197695-7696	0.98	2455351.2381	70	9.36 ± 1.08	DIFF2	
	1342197659-7660	0.98	2455350.4406	100	15.62 ± 1.22	DIFF1	This work
	1342197697-7698	0.98	2455351.2592	100	19.58 ± 1.22	DIFF2	
	1342197657-7660	1.96	2455350.4300	160	22.09 ± 2.76	DIFF1	This work
	1342197695-7698	1.96	2455351.2485	160	17.99 ± 2.76	DIFF2	
			Spitzer				
MIPS	13803776	0.41	2453542.2035	24	0.323 ± 0.049	BCD/MAIC	This work
	13803264	0.41	2453543.4306	24	0.384 ± 0.095		
	13803776	0.41	2453542.2035	70	13.48 ± 3.47	BCD/MFILT	This work
	13803264	0.41	2453543.4306	70	15.12 ± 2.79		
MIPS	19179264-6448	7.584	2454257.1740	24	$0.295 \pm 0.025^*$	BCD/MAIC	This work
	19179264-6448	7.584	2454257.1740	70	$11.17 \pm 0.50^*$	BCD/MFILT	This work
			ALMA				
ALMA		0.31	2457449.79514	1300	1.185 ± 0.085		L17

Note. The columns list the instruments, AORKEYs/ObsIDs, midtimes (Julian Date), in-band flux densities (F^i), data product type, and source of the photometric data. The SPIRE color-correction factors are 0.945, 0.948, and 0.943 at 250, 350, and 500 μm, assuming a blackbody SED in the Rayleigh–Jeans regime. Summary of flux densities of Makemake obtained in previous evaluations and in this work. L17 is E. Lellouch et al. (2017); measurements marked by an asterisk are the mean values of the long Spitzer measurements.

investigation. In addition to the MIRI photometric measurements, Makemake was identified on the target acquisition image of the MIRI/low-resolution spectrometer (LRS) measurement V01254001001P0000000002101, obtained with the F560W filter. Aperture photometry provided an aperture-corrected flux density of 58 ± 3 μJy.

Appendix C
Possible Contaminating Sources and Color-correction Effects

As Makemake seems to be significantly brighter than expected, especially in the JWST MIRI F1800W filter, we investigated the probability that the JWST measurements may be contaminated by another source. First, we checked the positional uncertainty of Makemake's orbit. According to JPL-Horizons, the astrometric 3σ uncertainties for the date of the JWST/MIRI observations are $\sigma_{R.A.} = 22$ mas and $\sigma_{decl.} = 15$ mas in R.A. and decl., respectively (i.e., Makemake is expected to be within these limits with 99.7% probability). Indeed, centroid fitting provides astrometry within $\lesssim$100 mas in all images to the predicted positions, which is much smaller than the $\sim$591 mas beam FWHM of the F1800W filter. To estimate the probability that an extragalactic source with the observed flux density is located within these uncertainties, we used the number count predictions by W. I. Cowley et al. (2018). For the F1800W filter, the expected number of sources $N(>150\,\mu\text{Jy}) = 0.5\,\text{arcmin}^{-2}$, and the corresponding probability that such a source is within the astrometric uncertainty is $p = 1.1 \times 10^{-6}$. Also, while Makemake moved $\sim 1''$ between the first F1800W and the last F2550W measurements (see Table 1), the fitted astrometric positions of the centroids remained consistent with the predicted positions of the target; i.e., we can safely reject the assumption that the source is an extragalactic or other sidereal source.

Two known asteroids ((400986) and 2021 KV_{111}) were identified in the relative vicinity of Makemake at the time of the JWST/MIRI observations, but both asteroids were at a safe

distance (>30″) from Makemake. Due to their higher surface temperature, small (undiscovered) main-belt asteroids in the few hundred meter size range may have F1800W and F2550W flux density values similar to the observed ones (see T. G. Müller et al. 2023 for a serendipitous detection of a similar main-belt asteroid with JWST). However, typical main-belt asteroids move with a speed of $\sim 0\farcs01\ s^{-1}$, which is clearly inconsistent with the observed movement. While a Centaur or a trans-Neptunian object could mimic the apparent motion of Makemake, it should be extremely large (at the top of the observed size range of these objects) to produce the observed flux densities. Therefore, we can safely consider the source observed with JWST/MIRI to be Makemake itself.

Due to the generally cold temperatures that are expected to be associated with the surface of Makemake, short-wavelength mid-IR filters in our analysis may experience large color-correction factors. Color corrections perform the transformation between the in-band and monochromatic flux densities: $F_m(\lambda) = F_i(\lambda)/C(\lambda)$, where $F_m(\lambda)$ and $F_i(\lambda)$ are the monochromatic and in-band flux densities, respectively, and $C(\lambda)$ is the wavelength- and SED-dependent color-correction factor, which accounts for the effect of an SED that is different from the reference SED used in the photometric calibration of the instrument (see, e.g., K. D. Gordon et al. 2022).

Based on the visible-range geometric albedo, the associated phase integral, and the heliocentric distance, Makemake is expected to have dayside average surface temperatures of ~40 K. In the case of a short-wavelength (mid-IR) excess with respect to that of these cold terrains, the mid-IR detectors will see higher effective temperatures. The color-correction factors of the mid-IR filters are relatively small ($C(\lambda) \lesssim 1.5$), although not negligible, for Makemake's typical surface temperatures ($T \approx$ 40 K), associated with a single-terrain model (see Section 2). For higher temperatures, $C(\lambda) \approx 1$; i.e., color corrections do not affect the mid-IR flux densities notably.

These calculations assumed a pure blackbody thermal emission. If there are no other sources but the cold surface of Makemake that contribute to the thermal emission, there is a considerable contribution from the reflected light of Makemake's surface to the mid-IR SED, especially at 18 μm (see Section 2). This makes the mid-IR JWST/MIRI F1800W and F2550W and the Spitzer/MIPS 24 μm color-correction factors much smaller than that of a single blackbody. In our models discussed above, all color-correction factors remain $C(\lambda) \lesssim 1.1$; i.e., they do not change the monochromatic flux densities considerably, and we can safely state that the high mid-IR flux densities cannot be explained by color-correction effects. In the thermal emission modeling (Section 2), color correction was considered for all filters, using the color-correction factors calculated from the actual (model) SEDs and the filter transmission curves.

To our knowledge, no filter leak has been identified for the MIRI F1800W or F2550W filters (see D. Dicken et al. 2024 for the evaluation of the MIRI imaging in-flight performance).

Appendix D
Thermal Emission Modeling

The shorter-wavelength mid-IR ($5\ \mu m \leqslant \lambda \leqslant 10\ \mu m$) light from Makemake is expected to be dominated by reflected light. The expected flux densities of the reflected light from Makemake were calculated for the observing geometry of the JWST/MIRI measurements using two methods. We first considered a $D = 1430$ km sphere at Makemake's heliocentric and observer distance and phase angle and using the NASA Space Science Institute solar reference spectra.[18] We also calculated it from the known absolute brightness and observing geometry with a wavelength scaling that corresponds to a 5780 K blackbody. The two calculations resulted in nearly identical reflected-light SEDs. The JWST/MIRI LRS target acquisition measurement provided an F560W band flux density of $F_{5.6} = 58 \pm 3\ \mu$Jy, which, when scaled to the solar reference spectrum, corresponds to a $p_{5.6} = 0.80 \pm 0.05$ albedo at 5.6 μm. We used this albedo value as representative of all $\lambda \geqslant 5\ \mu$m wavelengths when considering the reflected-light contribution in thermal emission calculations.

To model the thermal emission of Makemake, we use an elliptical NEATM model (A. Farkas-Takács et al. 2020); however, the potentially nonspherical shape of Makemake plays only a small role. As it has been previously suggested by J. L. Ortiz et al. (2012) and M. E. Brown (2013), the apparent axis ratio of Makemake, as obtained from the occultation chords, is $a'/b' \lesssim 1.05$. Also, using the mass of Makemake (A. Parker et al. 2018), the occultation size, and the rotation period of $P = 11.4$ hr, a Maclaurin spheroid—the shape of a rotationally deformed strengthless body held together by gravity—would have a true axis ratio of $a/c \approx 1.05$, which translates into the same apparent axis ratio ($a'/b' \approx 1.05$) as in the case of an equator-on geometry. Using this axis ratio, the largest possible apparent semiaxes are $a' = 751$ km and $b' = 715$ km. This leads to an SED that is only slightly, ~2%–4%, different from the spherical case of $a' = b' = 715$ km, as obtained from the occultation results. Therefore, in the following, we consider a spherical Makemake in the thermal emission modeling.

Some of the scenarios we investigate here have been considered in A. H. Parker et al. (2016) and E. Lellouch et al. (2017), but here we use additional thermal emission data, updated flux densities, and different ancillary data (e.g., new phase integral values) than in these previous papers.

Case 1: single-terrain Makemake. First, we considered Makemake to have a single-terrain surface with a geometric albedo of $p_V = 0.82 \pm 0.02$ and a phase integral of $q = 0.90 \pm 0.05$ and therefore a Bond albedo of $A_B = 0.74 \pm 0.06$ (A. J. Verbiscer et al. 2022). We assume that the surface is homogeneous, and no other component in the system contributes to the thermal emission. We calculated NEATM models using beaming parameters of $\eta = 0.6$–2.6 (E. Lellouch et al. 2013), presented as gray curves in Figure 1(a). The thermal emission model of $\eta = 1.2$, the mean value among trans-Neptunian objects (J. Stansberry et al. 2008; E. Vilenius et al. 2012; E. Lellouch et al. 2013), fits the observed flux densities very well for $\lambda \geqslant 160\ \mu$m.

Case 2: single-terrain Makemake + dark satellite. Makemake has a satellite that may contribute significantly to the thermal emission in the mid-IR and at the shorter far-IR wavelengths, as discussed previously by A. H. Parker et al. (2016) and E. Lellouch et al. (2017). The satellite is 7.8 mag fainter than Makemake (A. H. Parker et al. 2016). The absolute magnitude of the Makemake system is $H_V = 0.049 \pm 0.020$ mag (T. A. Hromakina et al. 2019); i.e., the satellite's absolute magnitude is $H_V = 7.85$ mag. This would correspond to diameters $D = 51$, 113, 160, and 253 km assuming geometric albedos of $p_V = 0.5$, 0.1, 0.05, and 0.02, respectively. The

[18] https://sunclimate.gsfc.nasa.gov/ssi-reference-spectra

satellite contribution is a very small correction on Makemake's absolute brightness; Makemake alone has $H_V = 0.050$ mag. The phase integral for Makemake is $q = 0.90 \pm 0.05$, and for a dark moon ($p_V \leqslant 0.05$), a typical phase integral in the trans-Neptunian region is $q = 0.26$, as determined by A. J. Verbiscer et al. (2022). We again used the NEATM model, as in the single-terrain case, assuming the same model for the bright terrain. In addition, we considered the thermal emission of the satellite assuming $p_V = 0.01$, 0.02, 0.04, and 0.08 and using a beaming parameter of $\eta = 0.6$ in all these cases. $\eta = 0.6$ is about the physically possible minimum value for the beaming parameter (E. Lellouch et al. 2013) and provides the highest surface temperatures (highest mid-IR flux density) for the same albedo. In addition, we also included the "extreme moon" model by E. Lellouch et al. (2017), which assumed $p_V = 0.017$ and $\eta = 0.34$. The results as presented in Figure 1(b).

Case 3: double-terrain Makemake. To test whether the warm, short-wavelength emission in the Makemake system could be explained by a dark terrain on the surface of Makemake, as suggested, e.g., by T. L. Lim et al. (2010), we also calculate double-terrain models. For all double-terrain configurations, we assume that the bright terrain (p_{V1}) is Eris-like and the dark terrain (p_{V2}) is either Charon-like or Quaoar-like. The relative contribution of these two terrains can be obtained according to the equation, neglecting the potential differences in scattering properties of the two terrains, $p_{V0} = \Omega_1 p_{V1} + \Omega_2 p_{V2}$, where p_{V0} is the global (observed, disk-integrated) geometric albedo of Makemake, p_{V1} and p_{V2} are the geometric albedos of the two terrains, and Ω_1 and Ω_2 are the relative areas of the two terrains ($\Omega_1 + \Omega_2 = 1$). Following J. L. Ortiz et al. (2012), we assume that the dark terrain is located around the subsolar latitude belt, which depends on the orientation of the axis of rotation. As discussed in M. E. Brown (2013), previous thermal emission constraints and the very small light-curve amplitude indicate that Makemake might be seen very close to a pole-on configuration, with an aspect angle of $\vartheta \approx 20°$. However, Makemake's satellite (A. H. Parker et al. 2016) passes very close to Makemake in the line of sight, indicating that the satellite orbit may be close to edge-on, also suggesting an edge-on rotational configuration in the case of a tidally evolved system. The properties of the terrains we use are summarized in Table 3 below.

A_B' of the Eris terrain is calculated using a synthetic reflectance spectrum of Eris, obtained by assuming pure CH_4 grains with a specific size distribution, as obtained by A. Alvarez-Candal et al. (2020). Bond albedo is calculated using a version of the B. Hapke (1993) reflectance model, used for modeling the low phase angle surface of Eris (C. A. Trujillo et al. 2005; R. Szakáts & C. Kiss 2023). This wavelength-dependent physical albedo is convolved with the solar irradiance spectrum to obtain the total power per surface area (W m^{-2}) reflected from the surface in the visible and near-IR range (0.3–3 μm). This provides $A_B' = 0.90$, clearly showing that the usual assumption of $A_B \approx A_V$ in asteroid thermal emission models does not hold in the case of the surface of Eris, which is highly reflective in the visible. For thermal emission modeling, the fraction of the power of the solar irradiation absorbed is $(1 - A_B')$, and we use this value for the Eris-like terrain. For all other terrains, we assume that the usual $A_B \approx A_V$ holds, and we use the A_B values obtained by A. J. Verbiscer et al. (2022) in the thermal emission modeling too.

As shown in Figure 1(c), all dark terrain types discussed above show very similar SEDs (green, yellow, and red stripes) if the same beaming parameter (η) is used. Models using terrains with $\eta = 1.0$ (or higher) underestimate the mid-IR flux densities while being roughly compatible with the long-wavelength ($\lambda \geqslant 70$ μm) flux densities.

Table 3
Properties of the Terrains Considered for the NEATM Thermal Emission Modeling of Makemake

Terrain (1)		p_V (2)	q (3)	$A_B(=A_V)$ (4)	A_B' (5)
Makemake	Single	0.80	0.90	0.74	0.74
Eris	Bright	0.96	1.04	1.00	0.90
Charon	Dark	0.42	0.60	0.25	0.25
Quaoar	Dark	0.11	0.52	0.057	0.057

Note. The columns are (1) name of the terrain, corresponding to the global properties of the bodies named; (2) V-band geometric albedo; (3) V-band phase integral; (4) Bond albedo obtained from visible band measurements; (5) Bond albedo used for thermal emission modeling. All values are obtained from A. J. Verbiscer et al. (2022) except the A_B' value of Eris, which is obtained from spectral modeling (see the text for details).

Appendix E
Dust Temperature

We calculated the possible equilibrium dust temperatures at the heliocentric distance of Makemake for a range of possible materials and grain sizes, obtained from the power balance between the absorbed solar radiation and thermal emission of the grains, using the equation

$$\frac{R_\odot^2}{r_h^2}\int_0^\infty B_\lambda(\lambda, T_\odot) Q_{\rm abs}(\lambda) d\lambda = \int_0^\infty B_\lambda(\lambda, T_d) Q_{\rm abs}(\lambda) d\lambda, \tag{E1}$$

where $R_\odot$ is the radius of the Sun, r_h is the heliocentric distance, $T_\odot$ is the temperature of the Sun's photosphere, $Q_{\rm abs}$ is the absorption coefficient of the grains, and T_d is the dust temperature. Absorption coefficients have been determined using *OpTool* (C. Dominik et al. 2021) for each specific single grain size and composition. We have considered different kinds of carbonaceous and silicate grains, as well as water ice. The estimated dust temperatures are presented in Figure 8.

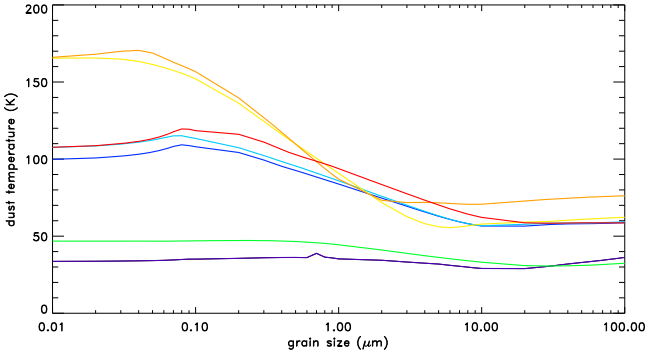

Figure 8. Dust temperature as a function of grain size for different compositions. Purple: pyroxene with 100% Mg content; blue: pyroxene with 40% Mg content; light blue: olivine with 50% Mg content; green: amorphous water ice; yellow: carbon grains as defined by V. G. Zubko et al. (1996); orange: graphite grains; red: "organic carbon."

Appendix F
Radiative Transfer Modeling of the Ring

Radiative transfer modeling of the dust grains in the ring is performed using RADMC-3D (C. P. Dullemond et al. 2012). The materials used for radiative transfer modeling are characterized by their composition, porosity, and size distribution. We use the *OpTool* package (C. Dominik et al. 2021) to obtain the absorption and scattering coefficients of the grains, using materials from *OpTool*'s material library and assuming a specific grain size distribution. We consider different types of materials in the different simulations, but we assume that the whole simulation volume is homogeneous material-wise. Anisotropic scattering is considered and treated by applying the Henyey–Greenstein function (option *scattering_mode_max=2* in RADMC-3D) and using the scattering opacity and g anisotropy parameters obtained for the specific material with *OpTool*.

We assume that an approximate ring model can be calculated by modeling the radiative transfer in a small element of the ring and simply multiplying the flux densities by the ratio of the ring area (A_r) to the area of the simulated region (A_s). The apparent area of the ring is

$$A_r = \pi((r_i + w)^2 - r_i^2)\sin B, \tag{F1}$$

where r_i and w are the inner radius and width of the ring and B is the opening angle. This model implicitly assumes that the ring is homogeneous and thin ($d \ll w$, where d is the thickness of the ring) and that edge effects are ignored. In detail, we used a $128 \times 128 \times 8$ cell simulation volume, which is illuminated under the proper solar geometry with respect to the ring and seen under the proper geometry from Earth (the smallest dimension corresponds to the vertical direction, perpendicular to the ring plane). The simulation volume is filled homogeneously with the actual material chosen.

The apparent, projected image of the simulated ring element is not homogeneous due to projection effects and has a lower intensity/optical depth toward the edges. However, it has the correct values in its central part, which correspond to the surface brightness values as if it were being seen in a homogeneous, full ring. We used those projected pixels for which $\tau = \max(\tau)$ in the visible-range R band, also calculated by RADMC-3D. We use this model to calculate both the reflected light and the thermal emission components. We assume that the ring is seen under an opening angle of $B = 15°$ and has a width of $w = 10$ km. Until the ring is optically thin, the ring width has a negligible effect on the final SED, but the observing and illumination geometry, including the B opening angle, is important, especially when calculating the reflected light, due to the directional dependence of the scattering.

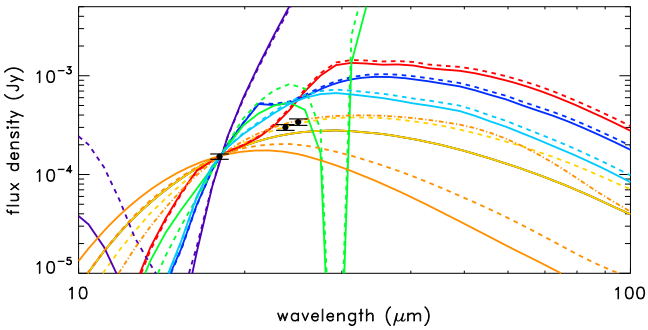

Figure 9. SED of different potential ring materials, normalized to the observed flux density at 18 μm (JWST/MIRI F1800W filter). The colors are the same as in Figure 8. Solid and dashed curves correspond to the same material but using 100 nm and 200 nm grain sizes, respectively. The orange dashed–dotted curve is for graphite grains with 500 nm grain size. The black symbols with error bars are the mean MIRI F1800W and F2550W and MIPS 24 μm flux densities.

Example SEDs of the ring, assuming different materials, are shown in Figure 9.

Appendix G
Grain Removal Timescales

We used the approach by J. A. Burns et al. (1979) to compute the evolution of dust grains around Makemake using a dynamical model, considering the gravitational field of Makemake and the Sun and the solar radiation pressure. The radiation pressure force component is obtained as

$$F_r = S_0(r_0/r_h)^2\pi s^2 c^{-1} Q_{\rm pr}, \tag{G1}$$

where S_0 is the solar constant, r_0 is 1 au, r_h is the heliocentric distance of Makemake in au, s is the grain radius, c is the speed of light, and $Q_{\rm pr}$ is the radiation pressure coefficient. $Q_{\rm pr}$ is calculated using the optical constants of the grains, as obtained in the previous calculations, and it is dependent on grain size and composition (see J. A. Burns et al. 1979 for a detailed discussion).

The effect of radiation pressure is modeled using a high-precision GPU-assisted Hermite N-body integrator (see K. Nitadori & J. Makino 2008; Z. Regaly et al. 2018), which takes into account the radiation pressure and the shadow cast on the ring by the dwarf planet. We performed the calculations for carbonaceous grains, different grain sizes, ring opening angles of $B = 0°$ and 15°, and initial ring radii corresponding to the 3:1 spin–orbit resonances assuming $P = 11.4$ or 22.8 hr. In the initial phase, the ring particles are in circular orbits around Makemake. In the case of a nonnegligible radiation pressure force, the photons radiated by the Sun perturb the particles' orbits, exciting their orbital eccentricity while maintaining their

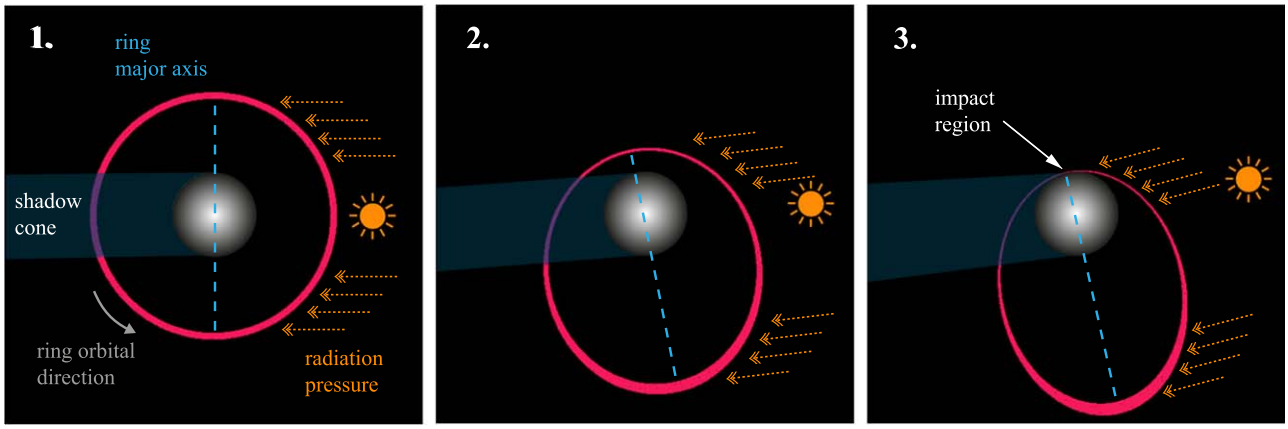

Figure 10. Time evolution (from left to right) of small grains around Makemake under the influence of solar radiation pressure.

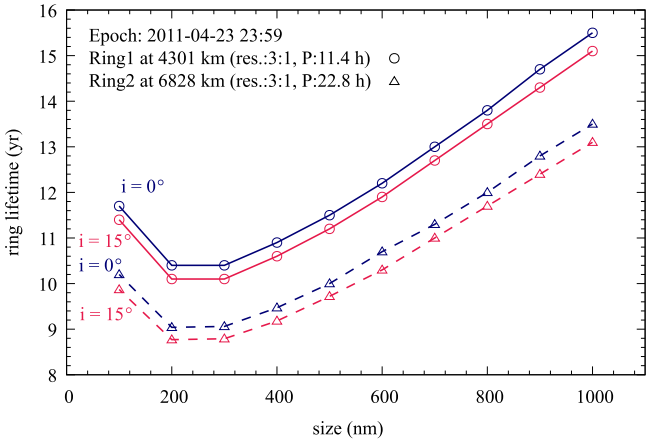

Figure 11. Lifetime of carbonaceous dust grains in the putative ring as a function of grain size. Curves with circle and triangle symbols mark the starting distances that correspond to the 3:1 spin–orbit resonances with $P = 11.4$ hr and 22.8 hr, while red and blue curves correspond to ring opening angles of 0° and 15°, respectively. We used Makemake's heliocentric distance at the time of the occultation on 2011 April 23.

semimajor axes (see Figure 10). As time progresses, the ring becomes globally eccentric, with the pericenter and apocenter points situated at the positions where the radiation pressure accelerates and decelerates the ring particles, respectively. Due to the relative direction of the Sun changing as a result of the orbital motion of Makemake, the ring's major axis experiences continuous tilting. In the end, the ring's eccentricity reaches a critical value, at which point $a_r(1 - e_{crit}) = R$, where R is the radius of Makemake's body; i.e., the pericenter of the ring particles reaches the surface of Makemake, and consequently, these grains are removed from the ring. As shown in Figure 11, small grains ($\leqslant 0.5\ \mu$m) around Makemake have lifetimes of ~ 10 yr, with some moderate dependence on the starting conditions (ring opening angle and starting semimajor axis).

ORCID iDs

Csaba Kiss https://orcid.org/0000-0002-8722-6875
Thomas G. Müller https://orcid.org/0000-0002-0717-0462
Anikó Farkas-Takács https://orcid.org/0000-0001-5531-1381
Attila Moór https://orcid.org/0009-0001-9360-2670
Silvia Protopapa https://orcid.org/0000-0001-8541-8550
Alex H. Parker https://orcid.org/0000-0002-6722-0994
Pablo Santos-Sanz https://orcid.org/0000-0002-1123-983X
Jose Luis Ortiz https://orcid.org/0000-0002-8690-2413
Bryan J. Holler https://orcid.org/0000-0002-6117-0164
Ian Wong https://orcid.org/0000-0001-9665-8429
John Stansberry https://orcid.org/0000-0003-2434-5225
Estela Fernández-Valenzuela https://orcid.org/0000-0003-2132-7769
Christopher R. Glein https://orcid.org/0000-0002-2161-4672
Emmanuel Lellouch https://orcid.org/0000-0001-7168-1577
Esa Vilenius https://orcid.org/0000-0002-6184-7681
Csilla E. Kalup https://orcid.org/0000-0002-1663-0707
Zsolt Regály https://orcid.org/0000-0001-5573-8190
Róbert Szakáts https://orcid.org/0000-0002-1698-605X
Gábor Marton https://orcid.org/0000-0002-1326-1686
András Pál https://orcid.org/0000-0001-5449-2467
Gyula M. Szabó https://orcid.org/0000-0002-0606-7930

References

Alvarez-Candal, A., Souza-Feliciano, A. C., Martins-Filho, W., Pinilla-Alonso, N., & Ortiz, J. L. 2020, MNRAS, 497, 5473
Balog, Z., Muller, T., Nielbock, M., et al. 2014, ExA, 37, 129
Bierson, C. J., & Nimmo, F. 2019, Icar, 326, 10
Braga-Ribas, F., Sicardy, B., Ortiz, J. L., et al. 2014, Natur, 508, 72
Brown, M. E. 2013, ApJL, 767, L7
Brown, M. E., Barkume, K. M., Blake, G. A., et al. 2007, AJ, 133, 284
Brown, M. E., Schaller, E. L., & Blake, G. A. 2015, AJ, 149, 105
Brown, R. H., Kirk, R. L., Johnson, T. V., & Soderblom, L. A. 1990, Sci, 250, 431
Burns, J. A., Lamy, P. L., & Soter, S. 1979, Icar, 40, 1
Bushouse, H., Eisenhamer, J., Dencheva, N., et al. 2024, JWST Calibration Pipeline v1.15.1, Zenodo, doi:10.5281/zenodo.6984365
Cowley, W. I., Baugh, C. M., Cole, S., Frenk, C. S., & Lacey, C. G. 2018, MNRAS, 474, 2352
Cuzzi, J. N., Filacchione, G., & Marouf, E. A. 2018, in Planetary Ring Systems. Properties, Structure, and Evolution, ed. M. S. Tiscareno & C. D. Murray (Cambridge: Cambridge Univ. Press), 51
Desch, S. J., Cook, J. C., Doggett, T. C., & Porter, S. B. 2009, Icar, 202, 694
Dicken, D., Marín, M. G., Shivaei, I., et al. 2024, A&A, 689, A5
Dominik, C., Min, M., & Tazaki, R., 2021 OpTool: Command-line Driven Tool for Creating Complex Dust Opacities, Astrophysics Source Code Library, ascl:2104.010
Dullemond, C. P., Juhasz, A., Pohl, A., et al., 2012 RADMC-3D: A Multi-purpose Radiative Transfer Tool, Astrophysics Source Code Library, ascl:1202.015
Farkas-Takács, A., Kiss, C., Vilenius, E., et al. 2020, A&A, 638, A23
Gaia Collaboration, Vallenari, A., Brown, A. G. A., et al. 2023, A&A, 674, A1
Giorgini, J. D., Yeomans, D. K., Chamberlin, A. B., et al. 1996, AAS/DPS Meeting, 28, 25.04
Glein, C. R., Grundy, W. M., Lunine, J. I., et al. 2024, Icar, 412, 115999
Gordon, K. D., Bohlin, R., Sloan, G. C., et al. 2022, AJ, 163, 267
Grundy, W. M., Wong, I., Glein, C. R., et al. 2024, Icar, 411, 115923

Guilbert-Lepoutre, A., Prialnik, D., & Métayer, R. 2020, in The Trans-Neptunian Solar System, ed. D. Prialnik, M. A. Barucci, & L. Young (Amsterdam: Elsevier), 183
Hamilton, D. P., Skrutskie, M. F., Verbiscer, A. J., & Masci, F. J. 2015, Natur, 522, 185
Hapke, B. 1993, Theory of Reflectance and Emittance Spectroscopy (Cambridge: Cambridge Univ. Press)
Harker, D. E., Wooden, D. H., Kelley, M. S. P., & Woodward, C. E. 2023, PSJ, 4, 242
Harris, A. W. 1998, Icar, 131, 291
Hedman, M. M., Postberg, F., Hamilton, D. P., Renner, S., & Hsu, H. W. 2018, in Planetary Ring Systems. Properties, Structure, and Evolution, ed. M. S. Tiscareno & C. D. Murray (Cambridge: Cambridge Univ. Press), 308
Henning, T., & Stognienko, R. 1996, A&A, 311, 291
Hofgartner, J. D., Birch, S. P. D., Castillo, J., et al. 2022, Icar, 375, 114835
Hofgartner, J. D., Buratti, B. J., Hayne, P. O., & Young, L. A. 2019, Icar, 334, 52
Hromakina, T. A., Belskaya, I. N., Krugly, Y. N., et al. 2019, A&A, 625, A46
Kargel, J. S. 1998, in Solar System Ices, ed. B. Schmitt, C. de Bergh, & M. Festou (Dordrecht: Kluwer), 3
Kiss, C., Müller, T. G., Marton, G., et al. 2024, A&A, 684, A50
Kiss, C., Müller, T. G., Vilenius, E., et al. 2014, ExA, 37, 161
Klaas, U., Balog, Z., Nielbock, M., et al. 2018, A&A, 613, A40
Lagerros, J. S. V. 1996, A&A, 310, 1011
Lagerros, J. S. V. 1998, A&A, 332, 1123
Lellouch, E., Moreno, R., Müller, T., et al. 2017, A&A, 608, A45
Lellouch, E., Santos-Sanz, P., Lacerda, P., et al. 2013, A&A, 557, A60
Lim, T. L., Stansberry, J., Müller, T. G., et al. 2010, A&A, 518, L148
Morgado, B. E., Sicardy, B., Braga-Ribas, F., et al. 2023, Natur, 614, 239
Müller, T., Kiss, C., Alí-Lagoa, V., et al. 2019, Icar, 334, 39
Müller, T., Lellouch, E., & Fornasier, S. 2020, in The Trans-Neptunian Solar System, ed. D. Prialnik, M. A. Barucci, & L. Young (Amsterdam: Elsevier), 153
Müller, T. G., Lellouch, E., Böhnhardt, H., et al. 2009, EM&P, 105, 209
Müller, T. G., Micheli, M., Santana-Ros, T., et al. 2023, A&A, 670, A53
Murray, C. D., & Dermott, S. F. 1999, Solar System Dynamics (Cambridge: Cambridge Univ. Press)
Nicholson, P. D., De Pater, I., French, R. G., & Showalter, M. R. 2018, in Planetary Ring Systems. Properties, Structure, and Evolution, ed. M. S. Tiscareno & C. D. Murray (Cambridge: Cambridge Univ. Press), 93
Nielbock, M., Muller, T., Klaas, U., et al. 2013, ExA, 36, 631
Nimmo, F., & Brown, M. E. 2023, SciA, 9, eadi9201
Nitadori, K., & Makino, J. 2008, NewA, 13, 498
Ortiz, J. L., Santos-Sanz, P., Sicardy, B., et al. 2017, Natur, 550, 219
Ortiz, J. L., Sicardy, B., Braga-Ribas, F., et al. 2012, Natur, 491, 566
Pál, A. 2012, MNRAS, 421, 1825
Pál, A., Kiss, C., Müller, T. G., et al. 2016, AJ, 151, 117
Pál, A., Szabó, R., Szabó, G. M., et al. 2015, ApJL, 804, L45
Pál, A., Szakáts, R., Kiss, C., et al. 2020, ApJS, 247, 26
Parker, A., Buie, M. W., Grundy, W., et al. 2018, AAS/DPS Meeting, 50, 509.02
Parker, A. H., Buie, M. W., Grundy, W. M., & Noll, K. S. 2016, ApJL, 825, L9
Pereira, C. L., Sicardy, B., Morgado, B. E., et al. 2023, A&A, 673, L4
Poglitsch, A., Waelkens, C., Geis, N., et al. 2010, A&A, 518, L2
Regaly, Z., Dencs, Z., Moor, A., & Kovacs, T. 2018, MNRAS, 473, 3547
Ricker, G. R., Winn, J. N., Vanderspek, R., et al. 2015, JATIS, 1, 014003
Rieke, G. H., Wright, G. S., Böker, T., et al. 2015, PASP, 127, 584
Rieke, G. H., Young, E. T., Engelbracht, C. W., et al. 2004, ApJS, 154, 25
Salo, H., & Sicardy, B. 2024, in Europlanet Science Congress 2024 (Göttingen: Copernicus GmbH) EPSC2024–1225
Sickafoose, A. A., & Lewis, M. C. 2024, PSJ, 5, 32
Singer, K. N., White, O. L., Schmitt, B., et al. 2022, NatCo, 13, 1542
Spencer, J. R. 1990, Icar, 83, 27
Spencer, J. R., Pearl, J. C., Segura, M., et al. 2006, Sci, 311, 1401
Stansberry, J., Grundy, W., Brown, M., et al. 2008, in The Solar System Beyond Neptune, ed. M. A. Barucci et al. (Tucson, AZ: Univ. Arizona Press), 161
Szakáts, R., & Kiss, C. 2023, PASP, 135, 124401
Tamayo, D., Burns, J. A., Hamilton, D. P., & Hedman, M. M. 2011, Icar, 215, 260
Tanga, P., Pauwels, T., Mignard, F., et al. 2023, A&A, 674, A12
Trujillo, C. A., Brown, M. E., Rabinowitz, D. L., & Geballe, T. R. 2005, ApJ, 627, 1057
Verbiscer, A. J., Helfenstein, P., Porter, S. B., et al. 2022, PSJ, 3, 95
Verbiscer, A. J., Skrutskie, M. F., & Hamilton, D. P. 2009, Natur, 461, 1098
Vilenius, E., Kiss, C., Mommert, M., et al. 2012, A&A, 541, A94
White, O. L., Moore, J. M., McKinnon, W. B., et al. 2017, Icar, 287, 261
Wright, G. S., Rieke, G. H., Glasse, A., et al. 2023, PASP, 135, 048003
Zubko, V. G., Mennella, V., Colangeli, L., & Bussoletti, E. 1996, MNRAS, 282, 1321